Review

Current trending and beyond for solar-driven water splitting reaction on WO₃ photoanodes

Magno B. Costa [a], Moisés A. de Araújo [b], Marcos V. de Lima Tinoco [a], Juliana F. de Brito [a,c], Lucia H. Mascaro [a,*]

[a] Departamento de Química, Universidade Federal de São Carlos, Rodovia Washington Luiz, km 235, São Carlos, São Paulo 13565-905, Brazil
[b] Instituto de Química de São Carlos, Universidade de São Paulo, Avenida Trabalhador Sancarlense, 400, São Carlos, São Paulo 13566-590, Brazil
[c] Instituto de Química, Universidade Estadual Paulista, Rua Professor Francisco Degni, s/n, Araraquara, São Paulo 14800-900, Brazil

ARTICLE INFO

ABSTRACT

This review shows the importance of WO₃ photoanode as a potentially low-cost, efficient, stable, and photoactive material for light-driven water splitting. For such, this manuscript aims to review the most recent publications regarding the strategies to improve the phoelectroactivity of WO₃ films for water oxidation. In addition, this review aims to graphically highlight and discuss the general trendings of the photocurrent density response and stability test of the recent outstanding studies in the literature for photoelectrochemical water splitting application. The strategies covered in this review will not only concern the WO₃ morphology and crystal plane growth, but also the many arrangements possibilities to improve the WO₃ efficiency for water photoelectrooxidation, such as defect engineering based on oxygen vacancies, doping, decorations, and homo and heterojunctions. All these strategies are compared by the photocurrent density results and by the stability of these photocatalysts. The best results in this sense were observed in cases where the use of heterojunction was applied together with a desired morphology and crystal plane of the WO₃ photoanode. However, the modifications that caused a decrease in the photocurrent density reaching values that are even lower than the pure WO₃ were also discussed. In this way, this review intends to improve the knowledge about the synthesis and design of WO₃ photoanodes to further obtain an efficient photocatalyst to minimize the recombination losses or losses across the interfaces and improve the photoelectroactivity for water splitting in the large-scale application.

© 2022 Science Press and Dalian Institute of Chemical Physics, Chinese Academy of Sciences. Published by ELSEVIER B.V. and Science Press. All rights reserved.

Magno B. Costa received his licentiate degree in Chemistry (2015) from the Instituto Federal do Espírito Santo (IFES), Brazil, and his MSc degree in Physical Chemistry (2017) from the Universidade Federal de São Carlos (UFSCar), Brazil. He is currently pursuing his PhD degree in Physical Chemistry at the UFSCar, Brazil, under the supervision of Prof. Lucia H. Mascaro. His research interests are focused on the synthesis and characterization of nanostructured semiconductor thin films for photoelectrochemical applications.

Moisés A. de Araújo received his BSc degree in Chemistry (2013) and MSc degree in Chemistry (2015) from the Universidade Federal do Ceará (UFC) and UFSCar, Brazil, respectively. He recently obtained his PhD degree in Science (concentration area: Physical Chemistry) (2020) from the UFSCar, Brazil, under the supervision of Prof. Lucia H. Mascaro. Currently, de Araújo is a postdoctoral fellow at the Universidade de São Paulo (USP), Brazil, working on the obtainment of chalcogenide-based semiconductor films for light-driven H₂ generation and photoelectrochemical CO₂ reduction. de Araújo's research interests include the synthesis and characterization of nanostructured semiconductor thin films for photoelectrochemical and photovoltaic cell applications.

* Corresponding author.
E-mail address: lmascaro@ufscar.br (L.H. Mascaro).
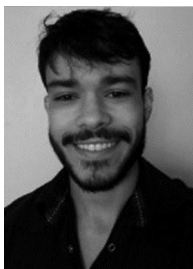
Marcos V. de Lima Tinoco is currently an undergraduate student in Chemistry at the UFSCar, Brazil, where he developed his undergraduate research project at the Laboratório Interdisciplinar de Eletroquímica e Cerâmica (LIEC), Brazil. The project focused on Pt deposition on Sb_2Se_3 thin films and its impact on the photoelectrochemical response for light-driven hydrogen evolution reaction. Additionally, Tinoco worked voluntarily at the Laboratório de Pesquisa em Eletroquímica (LAPE), Brazil, focusing on the synthesis of magnetic photocatalysts for the degradation of organic dyes.

Lucia H. Mascaro has been a professor in the Department of Chemistry at the UFSCar, Brazil, since 2006. She holds an MSc degree (1988) and a PhD degree (1992) in Chemistry, both from the UFSCar, Brazil. She was a postdoctoral fellow at the USP, Brazil (1994-1996), and the University of Bath, United Kingdom (2013-2014). Mascaro's research topics include corrosion, (photo)-electroanalysis, and preparation and characterization of semiconductor materials as well as metals and alloys for (photo)electrochemical water splitting and photovoltaic cell applications.

Juliana F. de Brito is a Temporary Lecturer at the UFS-Car, Brazil, and has recently been appointed as a professor at the Universidade Estadual Paulista (UNESP), Brazil. She concluded her PhD in 2018 from the UNESP, Brazil, and did her postdoc at the LIEC, Brazil until 2021 with research based on CO_2 reduction, N_2 reduction, and semiconductor development. The researcher has extensive experience in the areas of Analytics, Electrochemistry, and Environmental Chemistry with emphasis on the development of semiconductors, in addition to working with materials characterization and analysis and quantification of products generated in reduction reactions using techniques such as liquid, gas, and ion chromatography.
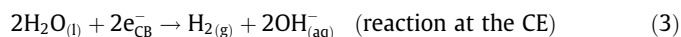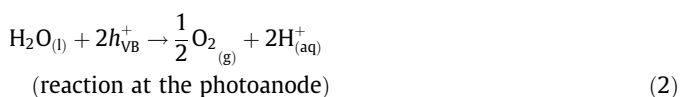
1. Introduction

The global environmental implications caused by the ever-growing use of fossil fuels have challenged scientists to develop new technologies to exploit alternative and clean sources of energy that above all can follow the twelve principles of green chemistry [1]. Among the new technologies being studied, photoelectrochemical (PEC) cells stand out as one of the most sustainable and promising approaches to obtaining a clean energy carrier, i.e., dihydrogen (H_2), via solar-driven water splitting [2,3]. By definition, a PEC cell is defined as a device for the conversion of radiant energy or solar energy into chemical energy, namely energy stored in chemical bonds. The basic configuration of a PEC cell consists of a photoelectrode, namely an n-type (photoanode) or p-type (photocathode) semiconductor, and a counter electrode (CE), which is usually a metal (e.g., Pt). These electrodes are immersed in an electrolyte containing a suitable redox pair and connected by an external circuit that may have an external bias to facilitate carrier separation [4]. Concerning the operation of a PEC cell for water photoelectrooxidation application (cf. Fig. 1), the first step consists of impinging light ($hv > E_g$) over a photoanode (n-type semiconductor) to photogenerate electrons in the conduction band (e_{CB}^-) and holes in the valence band (h_{VB}^+), Eq. (1) [5].

$$2hv \rightarrow 2e_{CB}^- + 2h_{VB}^+ \tag{1}$$

where hv is the photon energy to generate e_{CB}^- and h_{VB}^+ in the photoanode.

Owing to the built-in electric field or the (quasi-)Fermi level gradient in the space charge region (SCR) of the photoanode and the additional bias input, the photogenerated e_{CB}^- and h_{VB}^+ are spacially separated by migration [5]. The h_{VB}^+ migrates towards the photoanode|electrolyte interface to oxidize water into dioxygen (O_2), Eq. (2), and the e_{CB}^- are transferred to the CE|electrolyte interface via the external circuit to reduce water to H_2, Eq. (3) (adapted from [4,6]).

$$H_2O_{(l)} + 2h_{VB}^+ \rightarrow \frac{1}{2}O_{2(g)} + 2H_{(aq)}^+$$

(reaction at the photoanode) $\tag{2}$

$$2H_2O_{(l)} + 2e_{CB}^- \rightarrow H_{2(g)} + 2OH_{(aq)}^- \quad \text{(reaction at the CE)} \tag{3}$$

Combining the half-reactions described by Eqs. (2) and (3) with Eq. (1), it is obtained the overall water splitting reaction as shown by Eq. (4).

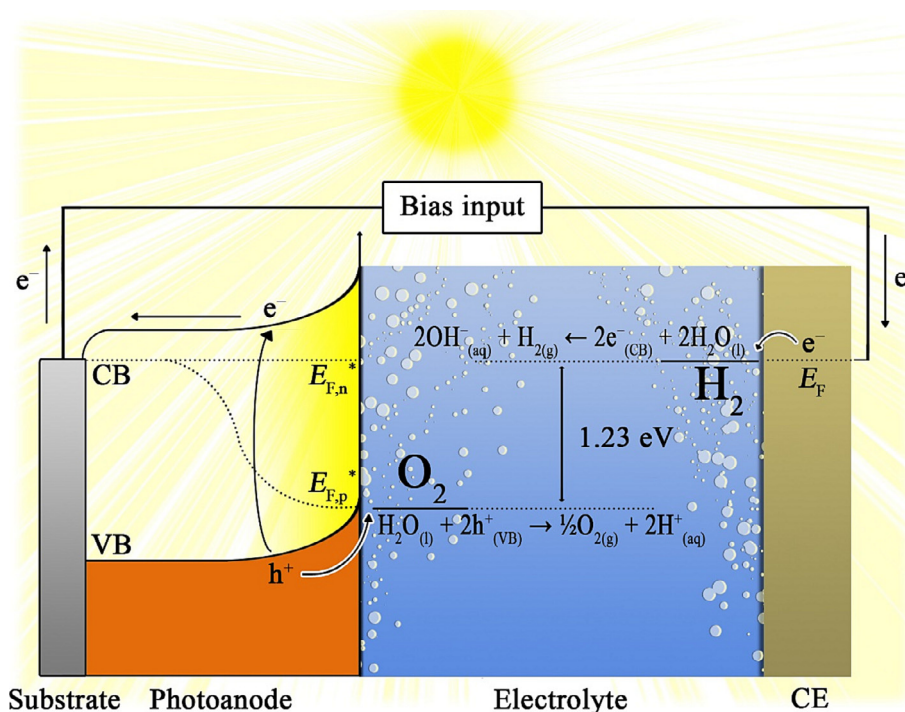$$2H_2O_{(l)} \xrightarrow{hv} 2H_{2(g)} + O_{2(g)} \tag{4}$$

At a neutral electrolyte, water oxidation and reduction have potential values of 0.83 and -0.40 V vs. standard hydrogen electrode (SHE) for the half-reactions given by Eqs. (2) and (3), respectively, and that provides an electrochemical cell voltage (ΔE) of -1.23 V for the overall water splitting reaction (see Eq. (4)). This ΔE can be correlated to the Gibbs free energy change (ΔG) of the overall water splitting process via Eq. (5) [7].

$$\Delta G = -nF\Delta E \tag{5}$$

where n is the number of electrons in the balanced electrode reaction (2 electrons) and F is the Faraday constant (96485.3 C mol^{-1}).

Employing Eq. (5) and considering the standard conditions (unit activity and pressure of 1 bar) and temperature of 298.15 K, one has a ΔG of 237 kJ mol^{-1} for the overall water splitting reaction [7]. Since the $\Delta G > 0$, this indicates that the overall process of splitting water into O_2 and H_2 (vide Eq. (4)) is non-spontaneous and requires at least an ΔE of -1.23 V for its occurrence. In terms of energy, it is equivalent to 1.23 eV, meaning that a semiconductor should theoretically feature bandgap energy (E_g) of 1.23 eV to light-driven water splitting [7]. However, for practical applications, the E_g should be higher than 1.23 eV to overcome the thermodynamic and kinetics losses [8]. Thermodynamic losses may be linked to several factors such as recombination and/or internal resistances to the transport of carriers in the semiconductor [9], while the kinetic losses are associated with the overpotential needed for the hydrogen evolution reaction (HER) and oxygen evolution reaction (OER) that take place at the electrode|electrolyte interface [10]. These overpotentials arise due to activation barriers for the elementary steps, mass transport in the solution phase, junction potential, and resistance to the flow of current inside the electrodes [11]. Taking into consideration all these losses, a semicon-

M.B. Costa, Moisés A. de Araújo, Marcos V. de Lima Tinoco et al.

Journal of Energy Chemistry 73 (2022) 88–113

Fig. 1. Schematic representation of a PEC cell comprised of a photoanode and a CE under operation in a generic neutral pH medium. VB is the valence band, CB is the conduction band, E_F is the Fermi level, and $E_{F,p}*$ and $E_{F,n}*$ are the quasi-Fermi level of holes and electrons, respectively.

ductor should have a E_g of approximately 2 eV to ensure that the overall solar-driven water splitting can proceed efficiently [10].

Another interesting topic to mention is that the occurrence of OER on a photoanode (see Eq. (2)) generates an anodic photocurrent density (Δj_{ph}) signal which can be used as a diagnostic tool to evaluate the PEC cell performance. In addition to the anodic Δj_{ph} response, there are efficiency metrics that can be employed to assess the PEC performance of a photoelectrode, namely photoanode or photocathode. Some of the efficiencies include the applied bias photon-to-current efficiency (ABPE), incident photon-to-current efficiency (IPCE), and absorbed photon-to-current efficiency (APCE), which are given by Eqs. (6), (7), and (8) [8], respectively. Strictly speaking, IPCE and APCE are identical to external quantum efficiency (EQE) and internal quantum efficiency (IQE), respectively.

$$\text{ABPE} = \left[\frac{|\Delta j_{ph}|(1.23 - E)\eta_F}{P_{total}} \right]_{AM1.5G} \quad (6)$$

$$\text{IPCE} = \text{EQE} = \frac{|\Delta j_{ph}|hc}{P_{mono}\lambda} \quad (7)$$

$$\text{APCE} = \text{IQE} = \frac{|\Delta j_{ph}|hc}{P_{mono}\lambda(1 - 10^{-A})} \quad (8)$$

where E is the applied bias or potential, η_F is the Faradaic efficiency, P_{total} is the irradiance (100 mW cm^{-2} for one sun condition), h is the Planck constant (6.626×10^{-34} J s), c is the speed of light (2.998×10^8 m s^{-1}), P_{mono} is the calibrated and monochromatic irradiance, λ is the monochromatic light wavelength, and A is the absorbance of the photoelectrode at a certain λ value.
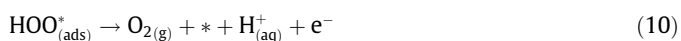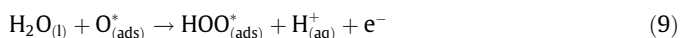
Even though the ABPE, IPCE, and APCE can provide useful information on the photoelectrode and interface properties, it is important to keep in mind that these efficiency metrics are only considered as diagnostics. For mainstream efficiency reporting, the only valid benchmark efficiency to characterize a PEC device

is the solar-to-hydrogen (STH) efficiency performed in a two-electrode cell configuration (i.e., working and counter electrodes) without polarization and under broadband solar irradiance (e.g., Air Mass 1.5 Global Illumination (AM1.5G)) [8].

Still concerning the OER on a photoanode, this reaction is usually considered the kinetic-controlling step for the overall water splitting reaction [12]. In this way, the development of a high-performance photoanode is utterly important for an outstanding PEC water splitting. For a highly efficient water photoelectrooxidation, it is also expected that the photoanode should meet the following requirements: (i) suitable optical E_g to harvest a wide range of energy from the solar spectrum; (ii) the valence band edge potential (E_{VB}) should be more positive than the OER potential (i.e., $E_{VB} > 0.83$ V$_{SHE}$, pH 7), while the conduction band edge potential (E_{CB}) should be more negative than the HER potential (i.e., $E_{CB} < -0.40$ V$_{SHE}$, pH 7); (iii) high efficient light absorption; (iv) fast and efficient carriers transfer at the photoanode|electrolyte interface; (v) diminished overpotential for the OER; (vi) stable at harsh conditions, such as acid/alkali electrolyte and under polarization and strong sunlight; (vii) the photoanode should not be toxic and be comprised of earth-abundant elements, and (viii) the preparation method for the photoanode should be inexpensive [4,7]. Despite there not yet a photoanode that can abide by all these requirements simultaneously, tungsten trioxide (WO₃) seems to meet most of the aforementioned criteria, which makes it a highly promising photoanode for PEC water splitting.

WO₃ is naturally an n-type semiconductor featuring a low-cost and non-toxic material with excellent photocatalytic activity on visible light radiation for water photoelectrooxidation applications [13]. Recently, Wang and co-workers have listed several intrinsic optoelectronic properties of WO₃, which indicates that this is a very attractive material compared to other photoanodes for solar-driven water splitting [4]. Some of the outstanding intrinsic properties of WO₃ photoanodes are: (i) suitable optical indirect E_g (2.5–2.8 eV [14]), which allows a collection of ~12% of solar energy for wavelengths <500 nm; (ii) high electron mobility (μ_e = 12 cm² V^{-1} s^{-1})

and moderate hole diffusion length ($\sim$150 nm) when compared to TiO_2 and α-Fe_2O_3 [15,16]; (iii) thermodynamically favourable position of the E_{VB} for water oxidation (i.e., E_{VB} is located at ca. 3 V_{SHE}, which is more positive than the oxidation potential of water (0.83 V_{SHE}, pH 7)) [17–19], and (iv) high chemical stability in acid medium and resistance to photocorrosion [20]. It is also important to highlight the water photooxidation mechanism on WO_3 photoelectrode, which is one of the main bottlenecks for the overall light-driven water splitting reaction. So far, very little has been known about the exact molecular reaction mechanism for water photooxidation reaction on WO_3 photoelectrode. Valdés and Kroes [21] proposed that the reaction mechanism for water photooxidation on WO_3 surface occurs in four steps as indicated by Eqs. (9)-(12). It was considered pH 0 for these reaction steps.

$$H_2O_{(l)} + O^*_{(ads)} \rightarrow HOO^*_{(ads)} + H^+_{(aq)} + e^- \quad (9)$$

$$HOO^*_{(ads)} \rightarrow O_{2(g)} + * + H^+_{(aq)} + e^- \quad (10)$$

$$H_2O_{(l)} + * \rightarrow HO^*_{(ads)} + H^+_{(aq)} + e^- \quad (11)$$

$$HO^*_{(ads)} \rightarrow O^*_{(ads)} + H^+_{(aq)} + e^- \quad (12)$$

where * is the site on top of a surface tungsten atom.

To propose these reaction steps, it was considered that the surface tungsten atoms were completely covered with adsorbed oxygen atoms (O^*), as this is the relevant surface for the photoelectrolysis process. Based on all these steps (see Eqs. (9) to (12), it is understood that the rate-limiting step for the oxidation process is the one described in Eq. (12), which is the proton transfer from the adsorbed hydroxyl radicals (HO^*) species to the electrolyte [21]. Backing up this information, it was evidenced experimentally by electron detection and spin trapping measurements of the formation of the $HO^\bullet$ radicals adsorbed on the surface of WO_3 aqueous dispersions under illumination [22]. Despite the actual molecular reaction mechanism not yet being fully unfolded, this theoretical study serves as a basis for future studies further understand more complex systems, such as photoelectrochemical water oxidation.

Regarding the physical properties and crystal structure of WO_3, this semiconductor is a yellow solid at room temperature that has an ABO_3 perovskite structure comprised of corner-sharing WO_6 octahedra (A = missing element and B = W) [12,23]. However, different syntheses of WO_3 reveal it with a distorted octahedral structure due to the antiferroelectric displacement of the W atoms and mutual rotations of the O octahedra [12], allowing the possible phases: tetragonal (α-WO_3), orthorhombic (β-WO_3), monoclinic I (γ-WO_3), triclinic (δ-WO_3), monoclinic II (ϵ-WO_3), and hexagonal (h-WO_3). Among all the polymorphic WO_3 crystals, the monoclinic phase I (γ-WO_3) is the most stable [14].

WO_3 was obtained for the first time by Robert Oxland in 1841 [24] and the application of WO_3 films as photoanode for water photoelectrooxidation was first reported by Hodes and co-works in 1976 [25]. In this work, the authors prepared the WO_3 films either by annealing the tungsten metal to form the W/WO_3 structure or by spraying ammonia tungstate onto a gold-coated glass substrate to obtain the glass/Au/WO_3 structure. Compared with TiO_2 films, the result of W/WO_3 film was very promising, presenting a high applied bias Δj_{ph} (ca. 1 mA cm^{-2} at 2.0 V vs. reversible hydrogen electrode (RHE)) and the onset potential (E_{on}) under illumination was shifted 1.4 V towards less positive values compared to the experiment performed in the dark. Despite this initial study presenting very promising results, there are still some limitations that prevent WO_3 photoanodes to achieve excellent PEC performance for large-scale applications. This is mainly due to the high recombination rate of the electron-hole pair and the slow transfer

kinetics of the photogenerated holes for water oxidation, leading to a poor and unsatisfactory transfer efficiency of the carriers at the WO_3|electrolyte interface [26]. In addition, peroxo species formed on the WO_3 surface during PEC water splitting can reduce the stability of WO_3 photoanode due to the photocorrosion process. Another drawback is that the reaction of peroxo species formation can compete with PEC water oxidation [19,27]. Another drawback is that the reported low absorption coefficient (α) of 10^4–10^5 cm^{-1} is assigned as the main cause for moderate hole diffusion length [28]. To overcome these issues, Zheng and co-workers [19] reported a variety of strategies to improve the WO_3 photoelectrocatalytic properties for PEC water splitting. The reported strategies which have recently been systematically classified as design principles [29] include as follow: (i) nanostructured morphology engineering to increase surface area, to minimize electron-hole recombination process, and to facilitate carriers migration towards semiconductor's surface [30]; (ii) photoanode superficial modification with suitable co-catalysts to accelerate PEC water oxidation reaction and to reduce the H_2O_2 production [11,31]; (iii) control of the exposed crystal facets at the semiconductor|electrolyte interface to enable facilitation of carriers transfer and high surface reactivity [32,33]; (iv) generation of chemical defects, such as oxygen vacancies, to act as adsorption centers for OH groups and as shallow electron donor [12,34]; (v) employment of doping approach to manipulate optical, electronic properties, and to tailor the electronic band structure of the semiconductor [35]; and (vi) preparation of homo/heterojunctions to allow photogenerated charge carriers to be separated and transported more efficiently [36–38].

All these strategies or also known as design principles have enabled recently considerable growth in the number of publications about WO_3 photoanodes applied to water photoelectrooxidation. Based on this, the present review aims to show the recent publications concerning the different strategies used to obtain WO_3 photoanode films for water oxidation. Moreover, we will provide graphic compilations of the published studies and additional comments for future works about how to further improve the photoelectroactivity of WO_3 photoanodes. To the best of our knowledge, this type of review comes as a novelty for the progress on the WO_3 photoanodes' studies toward PEC water splitting large-scale application in the future. To help the reader, this review was organized into two main topics, namely bare and modified WO_3 photoanodes. For these topics, we will present the strategies reported aiming to improve PEC performance and stability for water splitting. These strategies for bare WO_3 photoanodes were summarized as morphology influence, crystal plane growth control, and defect engineering based on oxygen vacancies; while for modified WO_3 photoanodes were: doping, surface modification, homojunction, and heterojunction approach. At the end of each section of this review, the main results of the reports discussed were organized in tables for comparative analyses.

2. Bare WO_3 photoanodes

2.1. Morphology influence

Morphology deals with the study of a material's form, which means the description of its shape, size, and structure [39]. In particular, the morphology of nanomaterials is uniquely important as it can dictate their physical-chemical properties. Different from bulk materials, the morphology of nanostructured materials plays a fundamental role in their photocatalytic activity. In addition to the material being nanostructured or bulky, the thickness of semiconductor materials, as well as the porosity [40], is also crucial for photocatalysis applications. To overcome the low α of WO_3, thicker films were produced, however, bulk materials with thicknesses
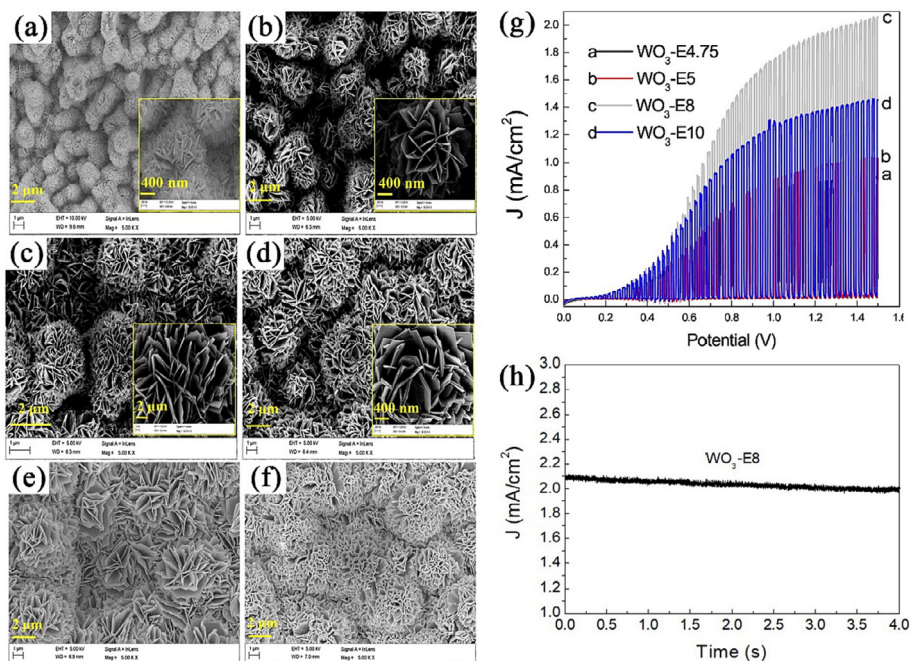
Fig. 2. (a–f) SEM micrographs and (g) linear sweep voltammograms at 50 mV s^{-1} and under chopped solar light simulator (AM1.5G and 100 mW cm^{-2}) for the WO$_3$ films obtained with different hydrothermal reaction times. (h) PEC stability at 1 V$_{Ag/AgCl}$ and under solar light simulator for (AM1.5G and 100 mW cm^{-2}) for the WO$_3$-E8 film. The electrolyte was a solution of 0.1 M Na$_2$SO$_4$. E4.75, E5, and E10 are the hydrothermal reaction times of 4.75, 5, and 10 h, respectively. Reproduced (adapted) from Ref. [46] with permission from Elsevier, Copyright 2019.

greater than the hole diffusion length imply a higher rate of electron/hole recombination before they can migrate to the semiconductor surface [28,30]. One of the advantages of nanostructured materials is the enlargement of the surface area. For the case of PEC cells, the enlarged surface area of a nanostructured semiconductor film enables more contact with the electrolyte, providing more active sites for carrying out PEC water splitting [41]. Nanostructured materials also show better light absorption due to reducing surface light reflection and increasing light scattering [42]. However, there are several disadvantages associated with the formation of nanostructures, such as a reduction in power conversion efficiency and a decrease in the durability of devices, in addition to many others directly related to PEC systems [43]. In other words, developing a photoelectrode from a given morphology directly influences its photoelectrocatalytic performance and, therefore, a relationship between them must be investigated. In this section, the influence of morphology on the PEC measurements of each system will be discussed based on the WO$_3$ obtaining methods, such as anodizing [44,45], a hydrothermal method [46–48], sol-gel [49–51], and pulsed laser deposition (PLD) [28,52].

The choice of substrate combined with the deposition method also plays an important role in morphology formation and consequently PEC performance. When it comes to transparent conductive oxides, several materials are used as substrates, such as fluorine-doped tin oxide (FTO), indium-doped tin oxide (ITO), and aluminium-doped zinc oxide (AZO), but only FTO is stable over a wide pH range [53]. Concerning the deposition method, one of the most common approaches for the manufacture of ordered oxide nanostructures is the anodization of metals. Several parameters associated with this method can influence, e.g., the morphology of WO$_3$. Zhang and co-workers manufactured nanoporous WO$_3$ films synthesized by tuning anodization conditions [44]. Parameters such as voltage and temperature of the electrolyte led to substantial morphological changes in the films, as they varied from compact to nanoporous structures that resemble nanotubes. From the optimized condition (anodizing tungsten foils at 40 V and 40 °C

and annealed at 500 °C in O$_2$ atmosphere), a Δj_{ph} of 1.1 mA cm^{-2} at 1.6 V$_{Ag/AgCl}$ and IPCE >40% in the UV region were obtained. Roselló-Márquez and co-workers employed the same manufacturing method and optimized the air-treated annealing conditions for the anodized films. The authors obtained WO$_3$ films featuring nanorods, which delivered a Δj_{ph} of ∼0.36 mA cm^{-2} at 1 V$_{Ag/AgCl}$ for the optimum annealing condition (600 °C in air) [45]. Although the synthesis conditions are similar to the previous study, the difference in photoactivity may be associated with the porous morphology of the obtained films. Porous structures have a larger surface area and a shorter diffusion length for the carriers that can facilitate the ions' transport into the structure and, consequently, improve the photoactivity of the film [54].

It is important to report that by employing the hydrothermal method, different 2D nanostructures were obtained for WO$_3$ films, such as nanoflowers, nanoflakes, and nanosheets. This difference in morphology allowed the Δj_{ph} to range from 1 to 2 mA cm^{-2}. Gu and co-workers prepared nanoflower structured WO$_3$ thin films (flower cluster diameters were ∼1 μm and the petal length was ∼200 nm) on Ti substrate with different hydrothermal reaction times (see Fig. 2a–f). This system delivered a Δj_{ph} of 2.0 mA cm^{-2} at 1.23 V$_{Ag/AgCl}$ and long-term stability of 4 h (Δj_{ph} decayed ∼5% from its initial value) for the film obtained with a hydrothermal reaction time of 8 h (labelled as WO$_3$-E8), as shown in Fig. 2(g and h), respectively [46]. The authors reported that the nanoflower structure was responsible for the enhanced PEC performance, which was attributed to the surface area enlargement for light absorption, an increase of reaction sites, and provision of more direct transfer channels for photogenerated electrons.

In another study, the control of morphology with the addition of ammonium oxalate ((NH$_4$)$_2$C$_2$O$_4$) in the synthesis method was also an important step in the work of Rong and co-workers [48]. The formation of WO$_3$ nanoflakes-like structure (thickness of 20–30 nm and 2.0 nm for amorphous layer) and the control of its structure parameters such as plate thickness and porosity by the addition of small amounts of (NH$_4$)$_2$C$_2$O$_4$ enabled the achieving a

M.B. Costa, Moisés A. de Araújo, Marcos V. de Lima Tinoco et al.

Journal of Energy Chemistry 73 (2022) 88–113
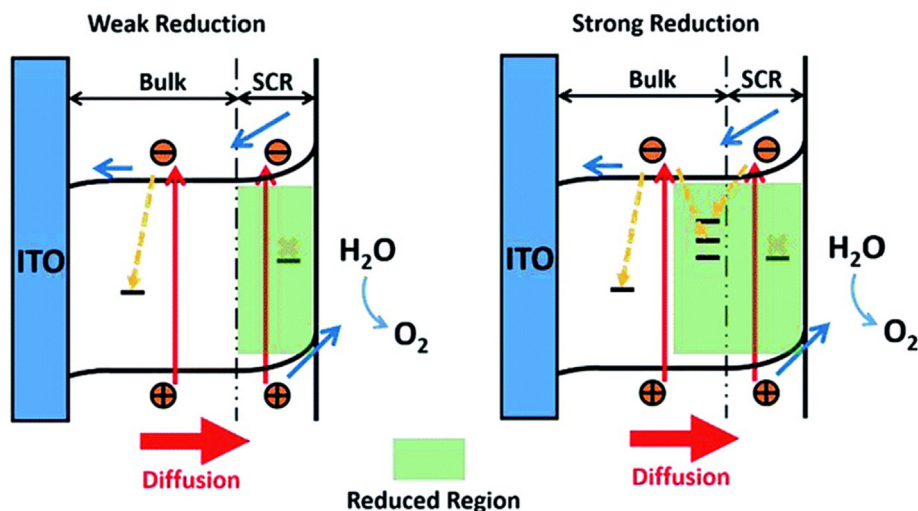
Fig. 3. Schematic band bending diagram and charge transfer processes in WO_3 photoanodes after weak and strong reduction treatments. Reproduced from Ref. [28] with permission from the Royal Society of Chemistry, Copyright 2019.

Table 1
Summary of bare WO_3 photoanodes featuring different morphologies for PEC water splitting.

Material	WO_3 fabrication method	WO_3 morphology	Electrolyte	Illumination	Notable PEC results	Ref.
W/WO_3	Anodizing	Nanopores	0.5 M Na_2SO_4	300 W Xe lamp AM1.5G 100 mW cm^{-2}	1.1 mA cm^{-2} at 1.6 $V_{Ag/AgCl}$ IPCE > 40% in the UV region	[44]
W/WO_3	Anodizing	Nanorods	0.1 M H_2SO_4	AM1.5G 100 mW cm^{-2}	~0.36 mA cm^{-2} 1 $V_{Ag/AgCl}$	[45]
Ti/WO_3	Hydrothermal	Nanoflowers	0.1 M Na_2SO_4	300 W Xe lamp AM1.5G 100 mW cm^{-2}	2.0 mA cm^{-2} 1.23 $V_{Ag/AgCl}$ IPCE ~40% at 380 nm (1 $V_{Ag/AgCl}$) Stability test for 4 h (decayed ~5%)	[46]
FTO/WO_3	Hydrothermal	Nanosheets	0.5 M Na_2SO_4	LED lamp AM1.5G 100 mW cm^{-2}	1.07 mA cm^{-2} at 1.23 V_{RHE} IPCE 82% at ~325 nm (1.23 V_{RHE})	[47]
FTO/WO_3	Hydrothermal	Nanoflakes	0.25 M PBS pH 6.5	Xe lamp AM1.5G 100 mW cm^{-2}	1.8 mA cm^{-2} at 1.23 V_{RHE} IPCE ~43% at 330 nm	[48]
FTO/WO_3	Sol-gel	Porous structures	1 M H_2SO_4	AM1.5G 100 mW cm^{-2}	2.05 mA cm^{-2} at 1.23 V_{RHE} IPCE 74.9% at ~380 nm Stability test for 10 h (decayed ~79%)	[49]
ITO/WO_3	Sol-gel	Porous structures	0.5 M Na_2SO_4	AM1.5G 300 mW cm^{-2}	0.97 mA cm^{-2} at 1.23 V_{RHE} IPCE 48.9% at 420 nm Stability test for 1.9 h (decayed 19.1%)	[50]
$PtSi/WO_3$	PLD	Columnar grain	0.5 M H_2SO_4	404 nm laser ~5 mW output power	29 mA cm^{-2} at 1.6 V_{RHE} APCE 7.7% at 404 nm (1.2 V_{RHE})	[52]
ITO/WO_3	PLD	Pyramidal	0.5 M H_2SO_4	150 W Xe lamp AM1.5G 100 mW cm^{-2}	1.81 mA cm^{-2} at 1.23 V_{RHE} E_{on} = 0.5 V_{RHE} IPCE, APCE ~95% at 340 nm (1.23 V_{RHE})	[28]
$ITO/N_2H_4-WO_3$	Squeegee method	Nanorods	0.1 M PBS pH 6	500 W Xe lamp 100 mW cm^{-2}	~0.9 mA cm^{-2} at 1.23 V_{RHE} IPCE 43.6% at 420 nm (1.05 V_{RHE})	[57]
FTO/WO_3	Fixed-potential deposition	Not informed	0.1 M Na_2SO_4	60 W tungsten lamp	~80–70 µA cm^{-2} at 1 $V_{Ag/AgCl}$	[58]
p-Si fronted solar cell/$CoSi_2$/WO_3	Co-electrodeposition	Not informed	1 M HCl	AM1.5G	~0.046 mA cm^{-2} without bias input	[59]
FTO/WO_3	Reverse nanoimprint lithography	Nanohole- and nanoline-patterned	PBS pH 7.6 + 1 M Na_2SO_3	AM1.5G	0.21 mA cm^{-2} at 1.23 V_{RHE}	[60]

high Δj_{ph} of 1.8 mA cm^{-2} at 1.23 V$_{RHE}$. On the other side, Zhao and colleagues synthesized a vertically aligned WO$_3$ nanosheet array and used electroreduction to form a disordered layer on the WO$_3$ surface [47]. This system provided a Δj_{ph} of 1.07 mA cm^{-2} at 1.23 V$_{RHE}$, and the IPCE has shown a high conversion value, reaching 82% at ∼325 nm.

Another synthesis method featuring a low cost for the preparation of bare WO$_3$ films is the sol-gel methodology, which enables obtaining semiconductor materials with nanoporous structures. Feng and co-workers obtained WO$_3$ films presenting the porous structure and small particle sizes with an average width of 35.4 nm, and these displayed highly reproducible and excellent photoelectrocatalytic performance for water splitting [49]. The obtained Δj_{ph} was 2.05 mA cm^{-2} at 1.23 V$_{RHE}$, with an average of 1.8 mA cm^{-2} after 50 randomly selected WO$_3$ samples and a low standard deviation (0.11 mA cm^{-2}). Wang and co-workers attributed the formation of WO$_3$ nanopore structures as the main factor in improving the PEC O$_2$ generation [50]. This structure also provided a more efficient mass transport during the PEC process and the production of more active sites on the surface of the photoelectrode as well as facilitation of the photogenerated carriers transfer. Another interesting aspect to point out is that the carrier dynamics for WO$_3$ films featuring porous structures have also been assessed. In this sense, Rodríguez-Pérez et al. [55] deposited porous WO$_3$ films with different thicknesses over FTO by screen printing. Concerning the PEC results, the intensity-modulated photocurrent spectroscopy indicated that the rate constant for charge transfer to the electrolyte phase is larger than for the surface recombination process in most of the applied potential range.

PLD has also been used to manufacture efficient and high-quality WO$_3$ photoanodes. This method is one of the deposition techniques with greater precision in the mass transfer of material from the target and excellent control of crystallinity and stoichiometry [52,56]. Andrei and co-workers employed PLD to deposit WO$_3$ films over Si (001) covered with platinum substrates, and this system proved to be quite stable in acid and alkaline media [52]. Using as a light source a laser diode (wavelength of

404 nm and output power of ∼5 mW) for the PEC experiments, the WO$_3$ with columnar-like morphology showed a Δj_{ph} of 29 mA cm^{-2} at 1.6 V$_{RHE}$ in an acid medium. The authors assigned the PEC high-performance to the improvement of the transfer and the separation rate of the photogenerated carriers that occurred in the (001) 2D columnar ordering structures of the monoclinic WO$_3$.

Cen and co-workers also used PLD to obtain very thin WO$_3$ films (thickness of 500 nm) with pyramidal-like morphology. This system enabled improving PEC performance by tuning the depletion region in the WO$_3$ films [28]. In terms of Δj_{ph} response for the OER, the WO$_3$ films having an optimized thickness of ∼500 nm provided a considerable Δj_{ph} of 1.81 mA cm^{-2} at 1.23 V$_{RHE}$. The authors associated the improved PEC performance to match the width of the depletion region with that of the reduction region (from post-annealing). In reduction regions larger than the depletion region, the sites of recombination eliminate the photogenerated charges (cf. Fig. 3).
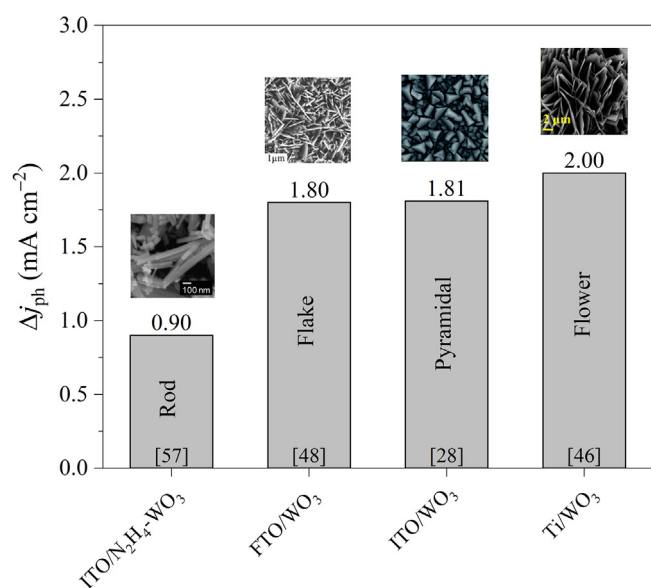
A summary of the most recent studies about the morphology effect on the photoelectroactivity of WO$_3$ films is listed in Table 1.

Aiming to compare the photoelectroactivity of the WO$_3$ films having different morphologies, some of the data in Table 1 were displayed in Fig. 4 for better visualization of the photoresponse trending. Firstly, it is important to clarify that a fair comparison of the compiled data in Fig. 4 is not possible due to the different electrolytes, substrates, synthesis methods, power of lamps used, and the variability of the surface properties (e.g., surface defects, vacancies, dangling bonds, impurities, etc.) of the WO$_3$ films. In this way, the summarized data in Fig. 4 can only provide a general trend, which is still useful as it can provide additional insights on how future works should spend more effort to further improve the PEC response of WO$_3$ films for large-scale applications.

Comparing the Δj_{ph} values at the standard water oxidation potential (1.23 V$_{RHE}$) for the different WO$_3$ morphologies presented in the literature (Fig. 4), one notices that the design of a particular morphology for this photoanode is intrinsically connected to its PEC response for water splitting reaction, and possibly respond to the yield in the H$_2$ production rate. WO$_3$ nanoflowers [46], pyramidal [28], and nanoflakes [48] morphologies presented the highest Δj_{ph}, reaching very similar values around 2.0 mA cm^{-2}, twice larger than the Δj_{ph} obtained for the nanorod [57] morphology. These studies show that not only the surface area obtained from the different morphology are responsible for the photoresponse improvement of the WO$_3$ films, but also the organization of the nanostructures is revealed to be crucial to increasing the Δj_{ph}, as highly organized or hierarchical nanostructures lead to high Δj_{ph}. In other words, obtaining WO$_3$ films featuring hierarchical nanostructures, such as nanoflowers, seems to be the best option to achieve a high PEC response for water oxidation. The high photoresponse for such structures is assigned to the combination of enlarged surface area and enhanced light absorption, as hierarchical nanoflowers can increase light absorption by the multiple reflections of the incoming light between the hierarchical nanostructures [61,62]. The nanorod structure can also behave as a light-trapping to increase incident light absorption via the multiple reflections within the nanorods. However, such a phenomenon is only possible for well-aligned and continuous nanorod arrays [63]. Since the reported WO$_3$ nanorods were not vertically standing [57], this may have hindered the benefit of light trapping and probably resulted in the relatively low Δj_{ph} as observed in Fig. 4.

Fig. 4. Δj_{ph} values at 1.23 V$_{RHE}$ for WO$_3$ photoanodes featuring different morphologies. Reproduced from Refs. [46] with permission from Elsevier, Copyright 2019, [57] with permission from American Chemical Society, Copyright 2019, [48] with permission from Elsevier, Copyright 2020, [28] with permission from Royal Society of Chemistry, Copyright 2019.

2.2. Crystal plane growth control

For the past two years, few studies have reported the use of strategy based on the preferential orientation of WO$_3$ crystallographic facets (texturing) applied to water photoelectrooxidation.
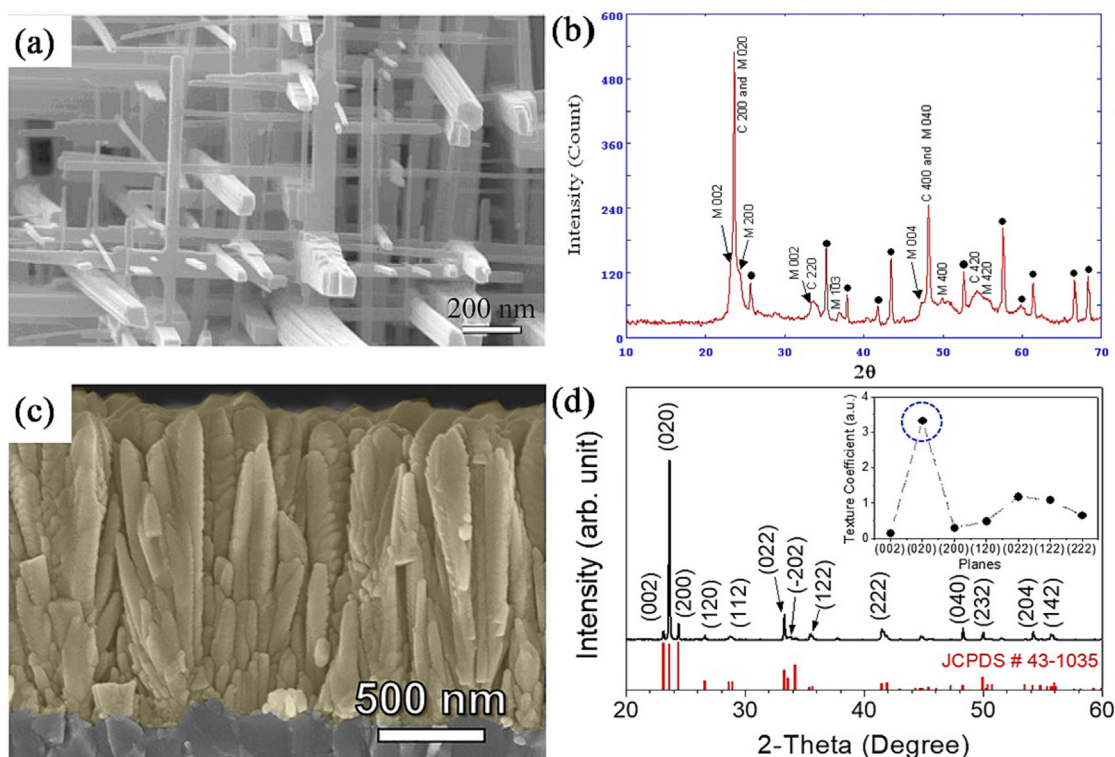
Fig. 5. (a) Nanowire networks and (c) columnar WO$_3$ nanostructure morphologies featuring preferential (020) facets determined from (b) and (d) XRD patterns, respectively. Reproduced from Ref. [66] with permission from Wiley-VCH, Copyright 2005, and Ref. [32] with permission from Elsevier, Copyright 2020.

Table 2
Summary of crystal plane control strategy for bare WO$_3$ photoanodes.

| Material	WO$_3$ fabrication method	WO$_3$ morphology	Electrolyte	Illumination	Notable PEC results	Ref.
FTO/(020)-textured WO$_3$	Laser ablation deposition	Columnar-type	0.5 M PBS pH 7	300 W Xe lamp AM1.5G 100 mW cm^{-2}	3.03 mA cm^{-2} at 1.23 V$_{RHE}$ IPCE 87% at 350 nm (1.23 V$_{RHE}$) Stability test for 2 h (decayed ~6%)	[32]
FTO/(002)-textured WO$_3$	Hydrothermal	Nanoplates	0.1 M Na$_2$SO$_4$	150 W Xe lamp AM1.5G 100 mW cm^{-2}	3.16 mA cm^{-2} at 1.23 V$_{RHE}$ IPCE 79% at 400 nm (1.23 V$_{RHE}$) Stability test for 5 h (decayed ~10%)	[33]
FTO/(002)-textured WO$_3$	Hydrothermal/ Doctor blade coating	Nanoparticles	0.5 M H$_2$SO$_4$	150 W Xe lamp LOT, Germany 100 mW cm^{-2}	3.5 mA cm^{-2} at 1.23 V$_{RHE}$ Stability test for 2 h (decayed ~15%)	[67]

The engineering of WO$_3$ crystallographic planes allows achieving improvement of the WO$_3$ film photoelectrocatalytic performances due to the exposure of the active facets. For WO$_3$ photoanodes, the facet (002) is the one with the highest surface energy (1.56 J m^{-2}) and is the most favourable one to receive reactive species to reduce on its surface when compared to facets (200) = 1.43 J m^{-2} and (020) = 1.54 J m^{-2} [64]. Theoretical studies based on density functional theory (DFT) calculations demonstrated that water photooxidation on γ-WO$_3$ surface demands an overpotential of 1.04, 1.10, and 1.05 V for the faces (200), (020), and (002), respectively [21]. In another theoretical study, Kishore et al. [65] reported that the (200), (020), (002) surfaces of WO$_3$ have a negligible effect on the overpotential for OER. The authors also reported that OER can be favoured on WO$_3$ surfaces with half coverage of oxygen atoms.

Besides the studies about crystal plane growth control, the occurrence of textured planes combined with the formation of nanostructures offers a large surface area for absorption and permeability of the electrolyte through the nanostructures of WO$_3$ films [32,66]. As an example, Fig. 5 shows two different nanostructures for WO$_3$ films with (020) facets determined from XRD data.

The combination of such features can potentially further improve the photoelectrocatalytic activity of WO$_3$ films for water photoelectrooxidation.

Han and co-workers employed laser ablation deposition to obtain WO$_3$ film featuring columnar nanostructures [32] (Fig. 5c). Unlike the acid medium commonly used in experiments involving WO$_3$ photoanodes, the authors chose to investigate the performance of the photoelectrode in a neutral medium as an ecological friendly pH conditions strategy. The control of synthesis operational conditions, such as temperature and pressure, allowed obtaining (020)-textured WO$_3$ films with a high number of oxygen vacancies. The occurrence of these vacancies leads to an increase in the charge transport in the semiconductor and better transfer efficiencies at the WO$_3$|electrolyte interface. Additionally, the control of the exposed facet combined with the amount of oxygen vacancy allowed the photoelectrode to reach a Δj_{ph} of 3.03 mA cm^{-2} at 1.23 V$_{RHE}$ and stability of 2 h (Δj_{ph} retention of 90%) in a neutral medium. In another study, Zheng and co-workers obtained sandwich structure based on (002)-textured WO$_3$ films. The facet of greater surface energy, i.e., (002), was grown by hydrothermal method and oriented via agent orientation (citric and tartaric acid) [33].
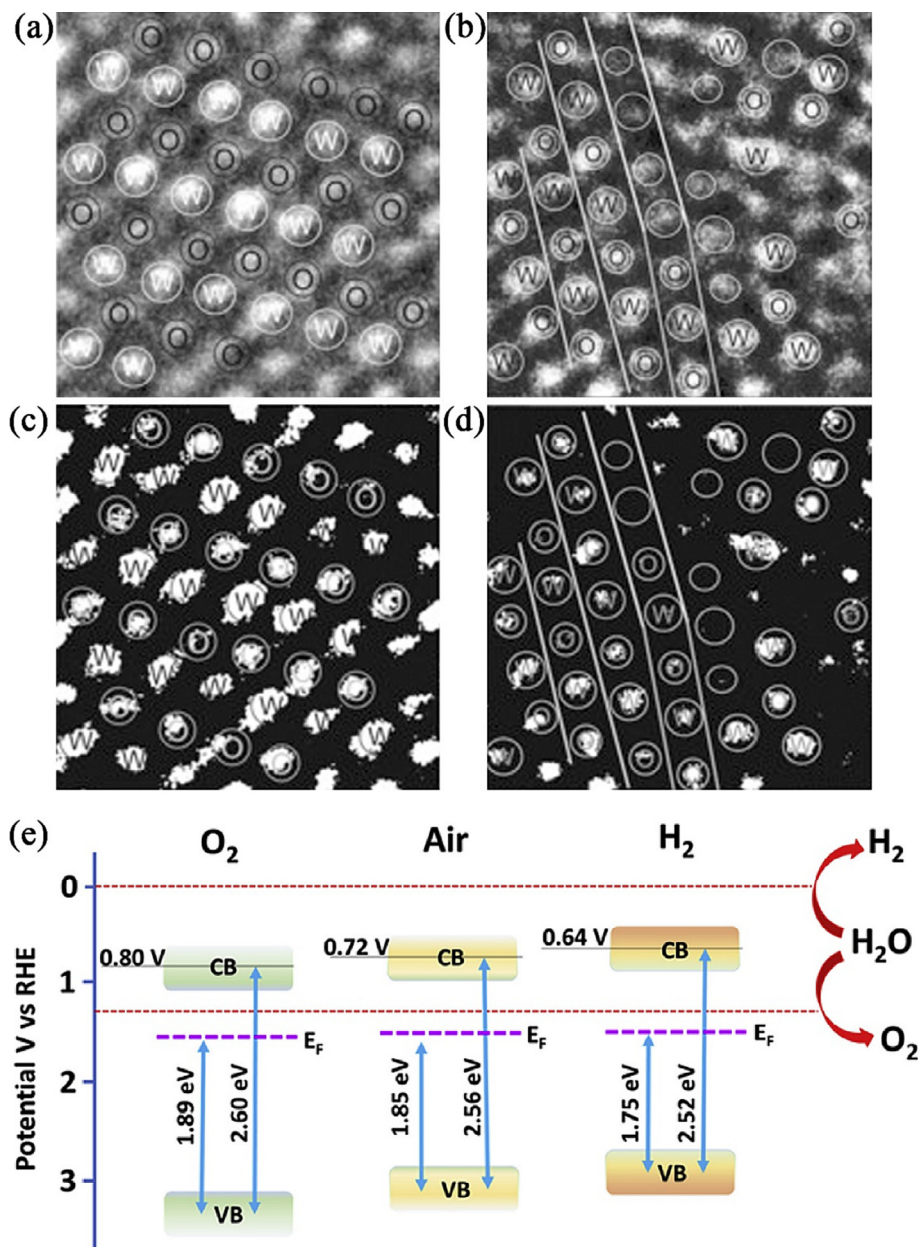
Fig. 6. (a and b) HRTEM and (c and d) HAADF images contrasting pristine WO$_3$ with continuous lattice fringes and with oxygen and tungsten deficiency. Reproduced from Ref. [72] with permission from Wiley-VCH, Copyright 2016. (e) Probable band edge positions of WO$_3$ photoanodes containing oxygen vacancies introduced via thermal treatment under O$_2$, air, and H$_2$ atmospheres. Reproduced from Ref. [78] with permission from Elsevier, Copyright 2019.

Table 3
Summary of defect engineering based on oxygen vacancies approach for bare WO$_3$ photoanodes.

Material	WO$_3$ fabrication method	WO$_3$ morphology	Electrolyte	Illumination	Notable PEC results	Ref.
FTO/WO$_3$ Oxygen vacancies	Hydrothermal	Nanoplates	0.5 M Na$_2$SO$_4$	Xe lamp 100 mW cm^{-2}	1.32 mA cm^{-2} at 1.23 V$_{RHE}$ IPCE 70% at 365 nm (1.23 V$_{RHE}$)	[76]
W/WO$_3$ Oxygen vacancies	Two-step flame heating	Nanoparticles	0.5 M H$_2$SO$_4$	AM1.5G 100 mW cm^{-2}	1.06 mA cm^{-2} at 1.23 V$_{RHE}$ E_{on} = 0.37 V$_{RHE}$ IPCE 47.9% at 390 nm (1.23 V$_{RHE}$) Stability test for ~1.7 h (approx. const.)	[77]
FTO/WO$_3$ Oxygen vacancies	Hydrothermal	Nanopores and blocks	0.1 M Na$_2$SO$_4$	1000 W Xe lamp AM1.5G 100 mW cm^{-2}	3.33 mA cm^{-2} at 2 V$_{RHE}$ IPCE ~50% at 400 nm (1.23 V$_{RHE}$) Stability test for 4 h (decayed 20%)	[78]
W/WO$_3$ Oxygen vacancies	Hydrothermal	Nanoplates	0.5 M Na$_2$SO$_4$	300 W Xe lamp AM1.5G 100 mW cm^{-2}	4.12 mA cm^{-2} at 1.6 V$_{Ag/AgCl}$ E_{on} = 0.22 V$_{Ag/AgCl}$ IPCE ~56.22% at 300 nm Stability test for 1 h (decayed ~5%)	[79]

The authors achieved a Δj_{ph} of 3.16 mA cm^{-2} at 1.23 V$_{RHE}$ and stability up to 5 h (Δj_{ph} decayed ∼10% from its initial value), which is so far one of the most notable results for pristine WO$_3$ films being no superficially modified or doped. According to the authors, both the preferred orientation of the (002) plane and the formation of WO$_3$ nanoplates contributed to the outstanding performance of the photoelectrode. Furthermore, the number of carboxylic groups of organic acids allowed for adequate texturing while the synergistic effect of the highly reactive exposed facet (002) and the 2D nanostructure facilitated the separation of photogenerated electron-hole pairs and suppressed the formation of peroxospecies [33].

In summary, these studies (listed in Table 2) show the possibility of obtaining highly efficient WO$_3$ films for PEC oxidation of water by simply controlling the texturing of planes. The facile and green hydrothermal method used by Zheng and co-workers [33] proved to be efficient and a step forward in the engineering of materials for energy conversion in PEC cells.

2.3. Defect engineering based on oxygen vacancies

The engineering of chemical defects in semiconductor materials is also considered an excellent strategy for boosting water splitting in PEC cells. Differently from physical defects (such as cracks and microsized holes) inside the semiconductor that could negatively interfere with the photocatalytic activity, chemical defects, such as oxygen vacancies, can contribute positively to the PEC activity of WO$_3$ films [68]. Such vacancies can act as adsorption centres for OH groups as well as shallow electron donors which are positive effects to promote an improvement in the PEC activity [12,34]. In addition, the DFT approach has shown strong dependence on the OER overpotential with the presence of oxygen vacancies and doping effect [65]. This dependency is economically attractive as the input energy, i.e., applied potential, used in the PEC water splitting can be minimized or compensated for the presence of a number of oxygen vacancies.

Recently, some strategies have been used to induce oxygen vacancies in semiconductor oxides, such as Ar-plasma-etched [69], radiofrequency hydrogen plasma [70], vacuum heat treatment [71], reducing reagents [72], thermal treatment in H$_2$ atmosphere [73], electrochemical reduction [74], and flame reduction [75]. Another way to induce the formation of oxygen vacancies is via a solution-based reducing agent, namely lithium dissolved in ethylenediamine [72]. Employing this approach and using high-resolution transmission electron microscopy (HRTEM) (Fig. 6a and b) and high-angle annular dark-field (HAADF) techniques (Fig. 6c and d), Ma and co-workers [72] were able to show the pristine WO$_3$ with continuous lattice fringes and with oxygen and tungsten deficiencies. In Table 3, it can be seen that studies in which oxygen vacancies were introduced by Ar plasma [76] and flame heating approach [77] enabled achieving Δj_{ph} of approximately 1.32 mA cm^{-2} and 1.06 mA cm^{-2} at 1.23 V$_{RHE}$, respectively.

In some other studies, an even higher photocatalytic performance was observed for WO$_3$ films in which oxygen vacancies were introduced by air annealing after hydrothermal treatment [78,79]. In this regard, Kalanur and co-workers reported that increasing the number of oxygen vacancies led to a decrease in the optical E_g, an increase in the density of carriers, and a significant upward shifting of the band edge positions (see Fig. 6e) [78]. This allowed the system to have a wider light-harvesting in the visible and infrared regions and more efficient charge transportation upon illumination. In terms of photoresponse, the photoanode showed a Δj_{ph} of 3.33 mA cm^{-2} at 2 V$_{RHE}$ and long-term stability of 4 h (Δj_{ph} maintained 80% of its initial value). In another study, Soltani and co-workers employed a metallic tungsten substrate to manufacture WO$_3$ films having dual oxygen and tungsten vacancies [79]. The prepared WO$_3$ films featured porous and uniform distribution of nanoplate structures that rendered a large surface area, which the authors attributed to being the one responsible for the efficient charge collecting capability. Additionally, not only the oxygen vacancies, but also its maximum number of W^{5+} states led to several improvements in the system, such as
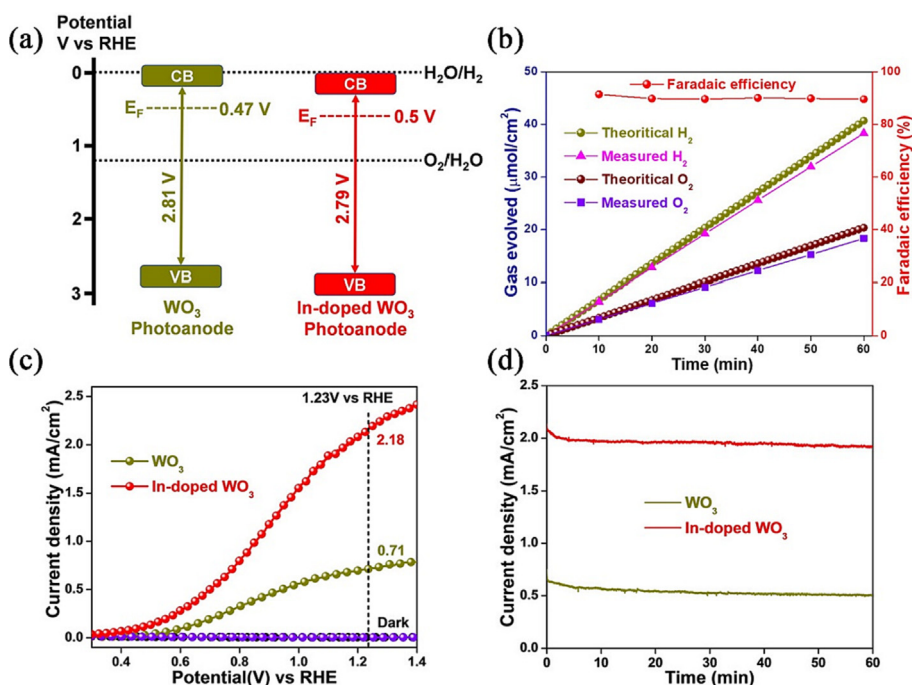
Fig. 7. (a) Position band edge potentials for bare WO$_3$ and In-doped WO$_3$ films, (b) Faradaic efficiency plot for In-doped WO$_3$ films, (c) linear sweep voltammograms at 10 mV s^{-1} in the dark and under solar light simulator (AM1.5G and 100 mW cm^{-2}), and (d) PEC stability at 1.23 V$_{RHE}$ and under solar light simulator (AM1.5G and 100 mW cm^{-2}) for bare WO$_3$ and In-doped WO$_3$ films. The electrolyte was an N$_2$-saturated solution of 0.1 M Na$_2$SO$_4$ at pH 6.0. Reproduced (adapted) from Ref. [85] with permission from Wiley-VCH, Copyright 2020.
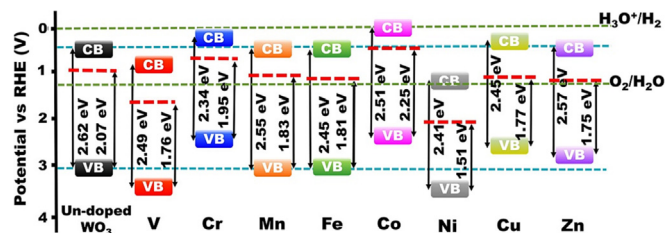
Fig. 8. Position band edge potentials for WO₃ films not doped and doped with different metals. Reproduced from Ref. [86] with permission from Elsevier, Copyright 2020.

Fig. 9. Δj_{ph} values at 1.23 V_{RHE} for Nb-, Ta-, Co–, and In-doped WO₃ photoanodes.

the decrease in the charge carrier resistances at the WO₃|electrolyte interface, an increase in the charge carrier concentration, and minimization the photogenerated electron-hole recombination. These improvements allowed the WO₃ films to reach a Δj_{ph} of 4.12 mA cm^{-2} at 1.6 $V_{Ag/AgCl}$ and stability of 1 h (the Δj_{ph} decayed 9% from its initial value).

3. Modified WO₃ photoanodes

3.1. Doping

Doping a semiconductor with metallic/non-metallic elements is a strategy used to manipulate its optical and electronic properties, and tailor its band structure [4,35]. In other words, doping can provide for a semiconductor: extension of the light range absorption, enhancement of the electronic transport capability, and desirable modification of the band edge positions [4]. For semiconductors having wide optical E_g energy, doping can also be used to narrow the separation between the energy bands, as in the case of, e.g., TiO₂ [80]; for semiconductors that are characterized by low electrical conductivity, such as Fe₂O₃, doping can increase the concentration of charge carriers and accelerate the kinetics of the oxidation reaction [81,82]; or even shift the maximum of the valence band and the minimum of the conduction band [83]. In addition, the doping of WO₃ films with isovalent elements normally limits the formation of defects such as vacancy due to the compatibility of the charges, while the doping with non-isovalent elements is generally compensated by the formation of oxygen vacancies [83,84].

Regarding the doping studies of WO₃ films for PEC water splitting application, it is reported a variety of doping elements, including In [85], first-row transition metal [86], and alkali ions [87]. Mohanta and co-workers reported that W⁶⁺ ions in the WO₃ struc-
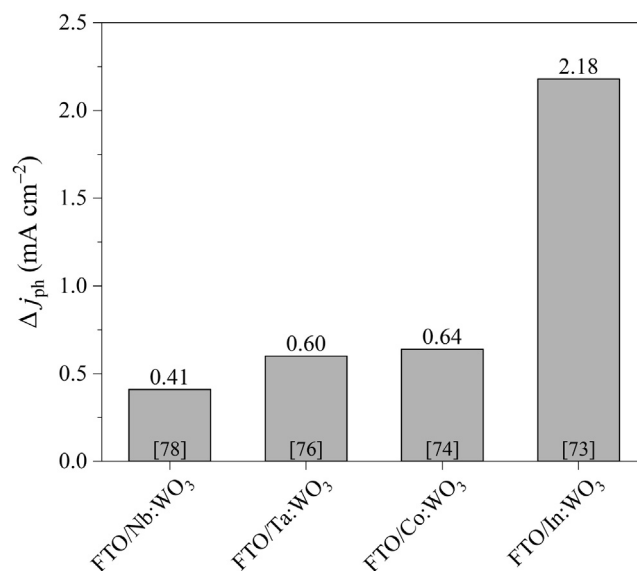
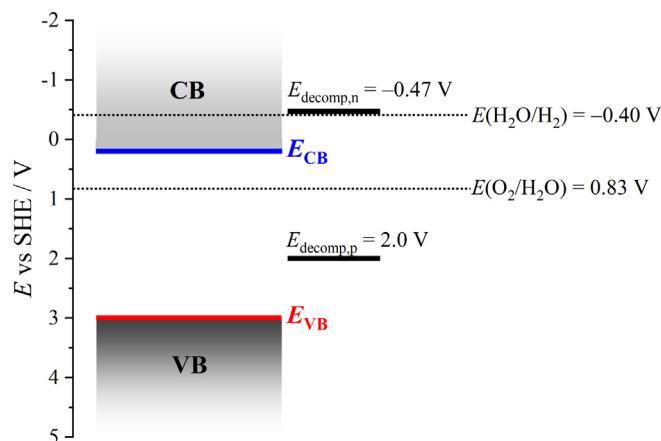ture were partially occupied by In³⁺ ions in the In:WO₃ system [85]. The authors achieved a significant increase in the density of charge carriers, which was three-fold greater than the undoped WO₃, and downward shifting of the CB and VB (see Fig. 7a). As a result, the η_F reached ∼90% for PEC water oxidation (cf. Fig. 7b), allowing a Δj_{ph} of 2.18 mA cm^{-2} at 1.23 V_{RHE} and stability of 1 h (decayed ∼5% from its initial value), as shown in Fig. 7(c and d), respectively.

Klamur and co-workers reported a systematic protocol for doping WO₃ films with a first-row transition metal (V, Cr, Mn, Fe, Co, Ni, Cu, and Zn). This study focused on the band edge engineering of WO₃ films to reduce the energy of E_g and alter band edge location (see Fig. 8) [86]. It was reported that the type of dopant directly influenced several properties of the WO₃ films, such as the crystalline phase, the density of the charge carrier, and the formation of oxygen vacancies. In contrast to the doping with V and Cr which decreased the PEC performance, all the other dopants promoted an improvement of the photoelectroactivity, especially the Co:WO₃ films, which presented the best Δj_{ph} of ∼0.64 mA cm^{-2} at 1.23 V_{RHE} and IPCE of 62.9% at 300 nm. Doping with Co resulted

Table 4
Summary of dopant elements employed for bare WO₃ photoanodes.

Material	WO₃ fabrication method	WO₃ morphology	Electrolyte	Illumination	Notable PEC results	Ref.
FTO/In: WO₃	Hydrothermal	Nanoblocks	0.1 M Na₂SO₄	AM1.5G 100 mW cm^{-2}	2.18 mA cm^{-2} at 1.23 V_{RHE} IPCE 42% at 373.7 nm (1.23 V_{RHE}) E_{on} = 0.5 V_{RHE} Stability test for 1 h (decayed ∼5%)	[85]
FTO/Co: WO₃	Hydrothermal	Nanorods and nanoparticles	0.5 M Na₂SO₄	1000 W Xe lamp AM1.5G	∼0.64 mA cm^{-2} at 1.23 V_{RHE} IPCE 62.93% at 300 nm (1.23 V_{RHE})	[86]
FTO/Li: WO₃	Doctor blade method	Spherical nanoparticles	0.2 M Na₂SO₄	500/150 W Xe lamp AM1.5G 100 mW cm^{-2}	0.43 mA cm^{-2} at 0.65 $V_{Ag/AgCl}$ IPCE 28% at 320 nm	[87]
FTO/Ta: WO₃	Hydrothermal	Nanotriangles	0.5 M Na₂SO₄	1000 W Xe lamp AM1.5G 100 mW cm^{-2}	∼0.60 mA cm^{-2} at 1.23 V_{RHE} IPCE ∼58% at 300 nm (1.23 V_{RHE})	[88]
FTO/Sn: WO₃	Hydrothermal	Nanoparticles and plates	0.5 M Na₂SO₄	1000 W Xe lamp AM1.5G	∼0.43 mA cm^{-2} at 1.23 V_{RHE} IPCE 44% at 300 nm (1.23 V_{RHE}) Stability test for 2.3 h (decayed ∼5%)	[89]
FTO/Nb: WO₃	Hydrothermal	Nanotriangles	0.5 M Na₂SO₄	1000 W Xe lamp AM1.5G 100 mW cm^{-2}	∼0.41 mA cm^{-2} at 1.23 V_{RHE} IPCE 52% at 300 nm (1.23 V_{RHE}) Stability test for 3 h (decayed ∼8%)	[90]
FTO/Cu: WO₃	Hydrothermal	Microsheets	0.5 M Na₂SO₄	Xe lamp AM1.5G 100 mW cm^{-2}	2.8 mA cm^{-2} at 1.23 V_{RHE} IPCE ∼35% at 340 nm (1.23 V_{RHE}) ABPE 0.27% at 1.0 V_{RHE} Stability test for 2 h (decayed ∼15%)	[91]

M.B. Costa, Moisés A. de Araújo, Marcos V. de Lima Tinoco et al.

Journal of Energy Chemistry 73 (2022) 88–113

Fig. 10. Band edge potentials positions and decomposition potentials for WO_3 in a generic neutral pH medium. $E_{decomp,n}$ is the WO_3's decomposition potential for reduction by electrons, $E(H_2O/H_2)$ and $E(O_2/H_2O)$ are the potentials for the cathodic and anodic decomposition of water, respectively. Adapted from Ref. [95].

in an upward shifting of the band edge positions, leading to a more suitable position for water oxidation. Additionally, the E_{on} was shifted to less positive values, which enabled to reduce the overpotential required for water oxidation. There was also a reduction in the E_g from 2.62 to 2.52 eV compared to the undoped WO_3 film. All these factors contributed to the Co doping being the best dopant among the others in the photocatalytic activity of WO_3 films.

In addition to the transition metal dopants, Yin and co-workers doped the WO_3 films with alkali ions by employing (Li, Na, or K)$_2SO_4$-based electrolyte [87]. According to the authors, the Li:WO_3 films provided the best PEC performance compared to the other alkali dopants (0.43, 0.35, and 0.37 mA cm^{-2} at 0.65 $V_{Ag/AgCl}$ for Li-, Na-, and K-doped WO_3, respectively). This was due to the reduced radius of Li$^+$ ions that facilitated their insertion into the WO_3 lattice and provided the best PEC performance among these dopants.

Another system being studied is the Ta-doped WO_3 which resulted in shifting the band edge positions and reduction of the optical E_g energy compared to the undoped WO_3 films. Additionally, there was an increase in the density of the carrier and the number of oxygen vacancies [88]. Other systems, such as Sn- [89] and Nb-doped [90] WO_3 have also produced similar effects, mainly by inducing downward shifting of the VB and CB as well as changes in the morphology and crystallographic orientation. Compared to the Sn and Nb dopants, Ta dopant enabled a partial or total change in the crystallographic phase of WO_3 films (from monoclinic/orthorhombic to hexagonal phase) due to the process of reconstructive transformation during annealing. The Ta:WO_3 system was also the one that provided the best PEC result (~0.60 mA cm^{-2} at 1.23 V_{RHE}), possibly associated with a combination of factors, such as charge carrier density higher than Sn:WO_3 and Nb:WO_3 films and low optical E_g value. A summary of the most recent studies about doping WO_3 films for PEC water splitting are listed in Table 4.

Seeking to observe a general trend of the WO_3 films photoresponse, Fig. 9 presents the Δj_{ph} reported in the literature at the standard water oxidation potential (1.23 V_{RHE}) for WO_3 photoanode doping with different metals. As already mentioned, the compilation of PEC data in Fig. 9 serves only to observe a possible trend and there is no intention to systematically compare these data due to the differences in surface characteristics, materials crystallinity and so forth. As shown in Fig. 9, the doping of WO_3 with In [85] was the most successful option reported in the literature, reaching
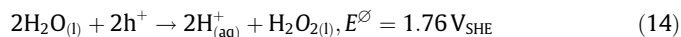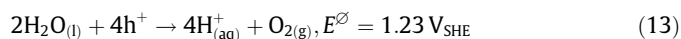
at least three times higher Δj_{ph} compared to the doping with Nb [90], Ta [88], or Co [86]. The insertion of 3% of In^{3+} in place of W^{6+} added additional charge carriers, amplifying the number of carriers' density in the photoanode. Based on these results, the enhancement of the photoelectroactivity of WO_3 photoanodes via doping with a well-chosen metal seems to be a more effective approach compared to the control of morphology, as can be observed comparing the results presented in Fig. 4 and 9. Although it may be a challenge, the combination of doping and the design of hierarchical nanostructures could be an alternative way to greatly improve the photoelectroactivity of the WO_3 photoanodes for water splitting.

3.2. Surface modification

For a large-scale application of PEC technology, several parameters must be dealt with equal importance to produce an efficient and viable device. Some of these parameters include cost-effective materials and techniques, photochemical performance, and stability [92].

The chemical instability of a photoelectrode, particularly, is one of the key points that can cause a device to become inefficient or inoperable at PEC *operando* conditions. Among the main metal oxides used as photoanodes, WO_3, ZnO, and Fe_2O_3 are the ones that present the most critical issues that directly affect their stability during the solar-driven water splitting process [93]. For WO_3 in particular, although this material is prone to anodic photodecomposition due to its decomposition potential for oxidation by holes ($E_{decom,p}$) is less positive than its E_{VB} (cf. Fig. 10), such process is hindered as a result of WO_3 being metastable, i.e., WO_3 is protected by the thermodynamically preferred decomposition of the electrolyte/solvent [94]. In other words, since the potential for anodic decomposition of the solvent, namely water oxidation, is less positive than the $E_{decomp,p}$ for WO_3 (see Fig. 10), the photooxidation of water on WO_3 occurs preferentially, which prevents triggering the anodic photodecomposition process of the WO_3 crystal [95].

Despite the WO_3 photoanodes being thermodynamically metastable against photocorrosion, it is important to mention that some factors still contribute to the WO_3 undergoing losses of its photoactivity during long-term stability. Wang and co-workers have listed two of the main causes of such losses [4,27,96]: (i) WO_3 can participate in an acid-base reaction due to its Arrhenius acid behaviour in an aqueous medium; and (ii) production of peroxo species during the oxidation of water, which can accumulate on the surface of the WO_3 photoanode and compromise its photocatalytic activity, i.e., slowing down the water oxidation kinetics. Thermodynamically, the OER via water oxidation process (cf. Eq. (13)) is more attainable than the formation of peroxo species (see Eq. (14)) [27,97].

$$2H_2O_{(l)} + 4h^+ \rightarrow 4H^+_{(aq)} + O_{2(g)}, E^\varnothing = 1.23\,V_{SHE} \tag{13}$$

$$2H_2O_{(l)} + 2h^+ \rightarrow 2H^+_{(aq)} + H_2O_{2(l)}, E^\varnothing = 1.76\,V_{SHE} \tag{14}$$

However, the slow kinetics of the OER can lead to the formation of peroxo species, which seems to kinetically compete with O_2 evolution [11,31]. This issue can be addressed by modifying the surface of WO_3 photoelectrodes with suitable oxygen evolution co-catalysts (OEC) to improve the kinetics of the OER. As a result, the presence of an OEC can suppress the formation of peroxo species, leading to an increase in the photostability of WO_3 as well as improvement of PEC O_2 generation.
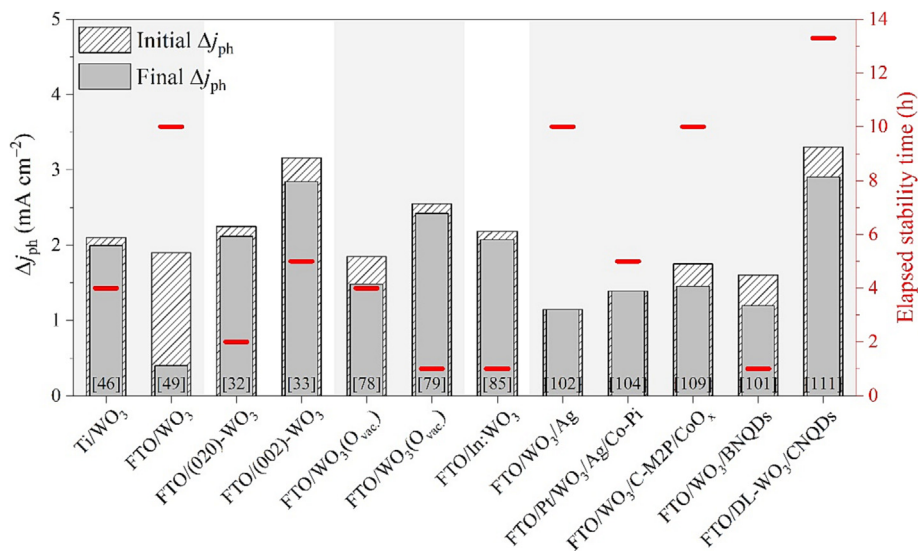
Recently, several types of co-catalysts have been used to modify the surface of WO_3 photoelectrodes, such as nanoparticles of noble metals [98,99], oxides [100], and quantum dots [101]. Li and co-workers prepared WO_3 films decorated with Ag nanoparticles pre-
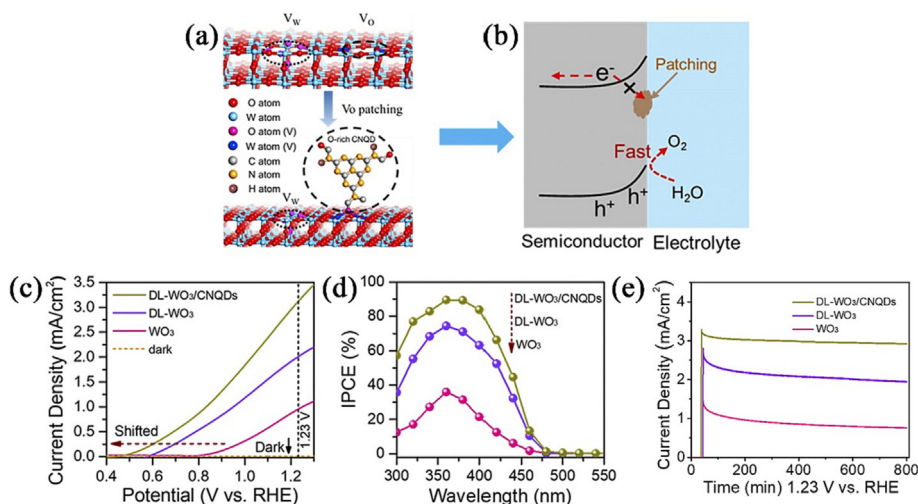
Fig. 11. (a) Schematic representation for the possible patching process of the surface DL (V_w and V_o are the W and O vacancy sites, respectively; O atom (V) and W atom (V) are the O atoms and W atoms around the vacancy). (b) Defect "patching" by non-passivating oxygen-rich CNQDs. The defect "patching" allows photo-induced holes to move towards the photoanode|electrolyte interface to directly oxidize water. (c) Linear sweep voltammograms in the dark and under solar light simulator (AM1.5G), (d) IPCE plots, and (e) PEC stability at 1.23 V_{RHE} and under solar light simulator (AM1.5G) for WO_3, DL-WO_3, and DL-WO_3/CNQDs films. The electrolyte was a solution of 0.5 M Na_2SO_4. Reproduced (adapted) from Ref. [111] with permission from Elsevier, Copyright 2019.

Table 5
Summary of surface modification approaches for WO_3 photoanodes.

Material	WO_3 fabrication method	WO_3 morphology	Electrolyte	Illumination	Notable PEC results	Ref.
FTO/WO_3/Ag	Solvothermal	Nanosheets	0.2 M Na_2SO_4	Xe lamp 100 mW cm^{-2}	1.15 mA cm^{-2} at 1.23 V_{RHE} ABPE 0.09% at ~1.1 V_{RHE} IPCE 57.8% at 330 nm Stability test for 10 h (approx. const.)	[102]
FTO/WO_3/Au	Solvothermal	Nanoflakes	0.5 M Na_2SO_3	300 W Xe lamp	1.01 mA cm^{-2} at 1.23 V_{RHE} IPCE ~45% at 300–470 nm	[98]
FTO/WO_3/Au	Hydrothermal	Plates	0.5 M Na_2SO_4	150 W Xe lamp AM1.5G 100 mW cm^{-2}	0.78 mA cm^{-2} at 1 $V_{Ag/AgCl}$ IPCE 57% at 300–400 nm	[103]
FTO/Pt/WO_3/Ag/Co-Pi	Hydrothermal	Smooth-faced nanorods	0.2 M Na_2SO_4	300 W Xe lamp AM1.5G 100 mW cm^{-2}	1.39 mA cm^{-2} at 1.23 V_{RHE} IPCE 40.8% at 380 nm Stability test for 5 h (approx. const.)	[104]
FTO/WO_3/PdO	Chemical vapor deposition	Nanoneedles	0.1 M H_2SO_4	AM1.5G 100 mW cm^{-2}	0.28 mA cm^{-2} at 1.23 V_{RHE} E_{on} = 0.55 V_{RHE} IPCE 49% at 325 nm (1.23 V_{RHE}) Stability test for 4 h (decayed ~12.5%)	[100]
FTO/WO_3/$CoFe_2O_4$	Hydrothermal	Nanoplates	0.1 M Na_2SO_4	AM1.5G	~0.035 mA cm^{-2} at 1.23 V_{RHE} E_{on} = 0.1 $V_{Ag/AgCl}$	[110]
FTO/WO_3/C-M2P/CoO_x	Hydrothermal	Nanosheets	0.1 M Na_2SO_4	LED 400 nm AM1.5G	3.5 mA cm^{-2} at 1.23 V_{NHE} IPCE 71% at 400 nm (1.23 V_{NHE}) ABPE 0.71% at 1.05 V_{RHE} Stability test for 10 h (decayed ~17%)	[109]
FTO/WO_3/ Mössbauerite	Hydrothermal	Nanoporous plate	0.1 M Na_2SO_4 + PBS	AM1.5G 100 mW cm^{-2}	1.22 mA cm^{-2} at 1.23 V_{RHE}	[113]
FTO/WO_3/BNQDs	Hydrothermal	Nanoblocks	0.1 M Na_2SO_4	250 W W lamp 100 mW cm^{-2}	1.63 mA cm^{-2} at 1.23 V_{RHE} IPCE 32% at 350–400 nm Stability test for 1 h (decayed ~25%)	[101]
FTO/WO_3/N:CDs	Hydrothermal	Nanoflakes	1 M H_2SO_4	500 W Xe lamp AM1.5G 100 mW cm^{-2}	1.42 mA cm^{-2} at 1 V_{SCE} IPCE 97% at 380 nm	[112]
FTO/DL-WO_3/CNQDs	Drop coating method	Nanopores	0.5 M Na_2SO_4	AM1.5G	3.1 mA cm^{-2} at 1.23 V_{RHE} E_{on} = 0.5 V_{RHE} IPCE ~90% at 350–400 nm (1.23 V_{RHE}) Stability test for ~13.3 h (decayed ~12%)	[111]
FTO/WO_3/Fh[a] ([a]Fh: Ferrihydrite)	Hydrothermal	Plate-like	0.5 M Na_2SO_4 pH 6.8	300 W Xe lamp AM1.5G 100 mW cm^{-2}	0.61 mA cm^{-2} at 1.23 V_{RHE} ABPE 0.066% at 1.05 V_{RHE} IPCE 20.7% at 350 nm (1.23 V_{RHE}) Stability test for 0.5 h (decayed ~15%)	[114]

M.B. Costa, Moisés A. de Araújo, Marcos V. de Lima Tinoco et al.

Journal of Energy Chemistry 73 (2022) 88–113

Fig. 12. Elapsed stability time and initial and final Δj_{ph} values were achieved before and after the stability test, respectively, at 1.23 V_{RHE} for the WO_3 photoanodes featuring the most recent modification strategies reported in the literature. The presented values of Δj_{ph} correspond to approximations based on the elapsed stability tests from their initial and final values.

pared by in situ cathodic reduction [102]. The presence of Ag nanoparticles enabled enhancing the separation of charges on the surface and improving the photoanode performance, which reached a Δj_{ph} of 1.15 mA cm^{-2} at 1.23 V_{RHE}. In addition, long-term photostability showed remarkable durability, remaining quite stable for 10 h under constant illumination. The presence of Au nanoparticles on WO_3 films has also shown interesting results, not only in the improvement of light-harvesting efficiency due to the effect of surface plasmonic resonance (SPR) but also in the charge separation at the interface [98,103]. Li and co-workers combined the SPR effect with the catalytic property of an OEC via superficial modification of the WO_3 films with Ag nanoparticles and an amorphous layer of cobalt phosphate (Co-Pi), respectively [104]. The Ag nanoparticles played a role in accelerating charge separation, while Co-Pi behaved facilitating the transfer of photogenerated holes to oxidize water into O_2. As a result, this system achieved a Δj_{ph} of 1.39 mA cm^{-2} at 1.23 V_{RHE} and improved photostability of 5 h during the experiment.
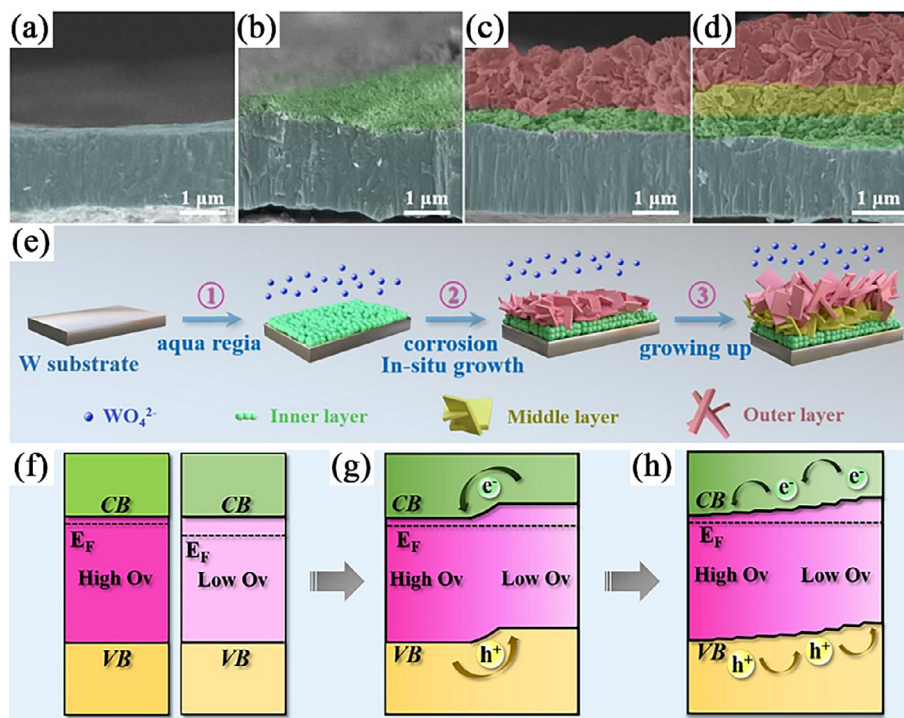
Although several co-catalysts have been used for the OER, for example, FeO_x [105], NiO_x [106], $B_2O_{3-x}N_x$ [107], and mainly Co-Pi [104]; so far, CoO_x has been one of the most efficient co-catalysts for promoting O_2 evolution [108]. In this regard, Hu and co-workers employed the organic linkage 3,3-diphosphonopropanate (C-M2P) to decorate the WO_3 films with the CoO_x co-catalysts, which resulted in obtaining the system $FTO/WO_3/C-M2P/CoO_x$ for PEC O_2 generation in neutral media [109]. The authors demonstrated that M2P favoured the migration of holes, enabling an efficient charge collection across the photoelectrode. This allowed the photoanode to reach a high charge carrier density value of 1.9×10^{23} cm^{-1} and passivation of the surface trap states. As a result, the WO_3 films superficially modified with C-M2P/CoO_x reached an incredible Δj_{ph} of 3.5 mA cm^{-2} at 1.23 V_{RHE} and an IPCE of 71% at 400 nm. In terms of photostability, the Δj_{ph} maintained ca. 85% of its initial value during 10 h of constant illumination. Based on these figures, the C-M2P layer played a crucial role in the performance of the PEC system, especially when compared to WO_3 films superficially modified with other oxide-based co-catalyst materials, such as PdO [100] and $CoFe_2O_4$ [110].

In another study, Jim and co-workers used oxygen-rich carbon nitride quantum dots (CNQDs) to patch the WO_3 nanoparticle disorder overlayer (DL-WO_3) since the presence of hole trapping sites harms the positive effect of oxygen vacancies toward WO_3 photoelectrocatalytic activity (Fig. 11a and b) [111].

The authors reported that oxygen-rich CNQDs can chemisorb on oxygen vacancies to repair the DL-WO_3 via interaction of $O^{-\delta}$ from the CNQDs with the $W^{+\delta}$ atoms surrounded by oxygen vacancies. The removal of surface charge trap sites allowed to achieve one of the best PEC performances so far for a WO_3/QD, which reached a Δj_{ph} of 3.1 mA cm^{-2} at 1.23 V_{RHE} and IPCE of 97% at 380 nm, as presented in Fig. 11(c and d), respectively. In addition, as shown in Fig. 11(e), this system presented incredible long-term stability of 13.3 h (Δj_{ph} decayed ~10% from its initial value).

This type of strategy involving the removal of oxygen vacancies has been recurrent in the past few years and its effect on the photoelectroactivity improvement of photoanodes based on metal oxides has been quite remarkable. Still concerning this type of strategy, other materials such as boron nitride quantum dots (BNQDs) [101] and nitrogen-doped carbon dot (N:CDs) [112] on WO_3 films enabled obtaining excellent results of Δj_{ph} response improvement for water oxidation. All in all, these studies indicate that the combination of co-catalysts on the WO_3 surface with the removal of oxygen vacancies in the bulk can be an excellent strategy to achieve even higher PEC performance and durability of WO_3 films for water oxidation. A summary of the most recent surface modification strategies for WO_3 films is listed in Table 5.

As presented so far, it is wide the possibilities to superficially modify the WO_3 films. Fig. 12 presents the most relevant results about substrate influence, crystal plane growth control, defect engineering based on oxygen vacancies, doping, and surface modification strategies for WO_3-based photoanodes as a function of the elapsed stability time and the Δj_{ph} response before and after stability test at 1.23 V_{RHE} which were referred to as initial and final Δj_{ph}, respectively. It bears repeating that the assembled PEC data in Fig. 12 aim to notice a possible general tendency of the results as a function of the modification strategies, systematic comparison is not intended here. Having that being clarified, according to Fig. 12, it is possible to point out that FTO may not be the best option as a substrate for the deposition of WO_3 films, as the final

M.B. Costa, Moisés A. de Araújo, Marcos V. de Lima Tinoco et al.

Journal of Energy Chemistry 73 (2022) 88–113

Fig. 13. (a-d) SEM micrographs for WO$_3$ photoanodes before and after reaction at 100 °C for 0.5, 1.5, and 3 h, respectively. (e) Schematic illustration of the growth mechanism of the sample WO$_3$-100 via the hydrothermal process in aqua regia. (f-h) Schematic illustration of the energy band diagrams for WO$_3$ films without homojunction, with homojunction, and distributed homojunction, respectively. For all cases, the W substrate is located on the left. Reproduced from Ref. [116] with permission from Elsevier, Copyright 2020.

Δj_{ph} was considerably smaller compared to the film grown on Ti substrate. Additionally, the crystal plane growth control deserves attention, the choice of a facet of the WO$_3$ can improve the Δj_{ph} by around 25%, comparing, for example, WO$_3$ [020] and WO$_3$ [002] [64]. Despite the broad options of surface modifications for WO$_3$ films, including the use of more than one layer of different metals, oxides and organics, in most cases, it did not bring an effective improvement in the Δj_{ph} for water splitting. Nevertheless, such superficial modifications allowed performing stability experiments for a longer period for, e.g., the FTO/DL-WO$_3$/CNQDs system [106], compared to the bare WO$_3$ photoanodes [11,32,46,49,74,75].

3.3. Homojunction-based WO$_3$ photoanodes

The combination of two or more semiconductors with different optoelectronic properties is an approach widely used in the PEC field to improve the photocatalytic performance of PEC cells. In particular, the homojunction approach, which is the combination

of two semiconductors having a similar composition and/or crystalline structure, can promote continuity of band bonding and, consequently, provide a better charge transfer at the semiconductor|electrolyte interface [37]. Such a system also features having a built-in electric field to produce an adequate gradient of carrier concentration and to promote bulk charge separation away from the sites that induce recombination [38].

Li and co-workers used the multijunction strategy combined with doping to improve the charge separation and transfer efficiency of WO$_3$ films [115]. The authors firstly obtained the FTO/Mo:WO$_3$/Fe:WO$_3$ based homojunction and then superficially modified it with nanoparticles of Bi$_2$S$_3$ (FTO/Mo:WO$_3$/Fe:WO$_3$/Bi$_2$S$_3$). The homojunction Mo:WO$_3$/Fe:WO$_3$ played an important role in the device performance since it showed an increase in bulk charge separation and transfer efficiencies, which was due to the occurrence of a built-in electric field or an enhanced (quasi-)Fermi level gradient at Mo:WO$_3$|Fe:WO$_3$ homojunction interface. The homojunction (Mo:WO$_3$/Fe:WO$_3$) provided additional improvement of

Table 6
Summary of homojunction-based WO$_3$ photoanodes for PEC water splitting application.

Material	WO$_3$ fabrication method	WO$_3$ morphology	Electrolyte	Illumination	Notable PEC results	Ref.
FTO/Mo:WO$_3$/Fe:WO$_3$/Bi$_2$S$_3$	Hydrothermal	Nanorods	0.2 M Na$_2$SO$_4$	Xe lamp AM1.5G 100 mW cm^{-2}	2.55 mA cm^{-2} at 1.23 V$_{RHE}$ ABPE 0.35% at 0.68 V$_{RHE}$ IPCE ~45% at 300–400 nm (1.23 V$_{RHE}$) Stability test for 2 h (decayed ~10%)	[115]
W/WO$_3$	Hydrothermal	Nanoplates	0.5 M Na$_2$SO$_4$	300 W Xe lamp AM1.5G 100 mW cm^{-2}	1.81 mA cm^{-2} at 1.23 V$_{RHE}$ IPCE ~62% at 380 nm (1.23 V$_{RHE}$)	[116]
FTO/1D-WO$_3$/2D-WO$_{3-x}$	Hydrothermal	Nanorods and nanoflakes	0.2 M Na$_2$SO$_4$	300 W Xe lamp AM1.5G 100 mW cm^{-2}	0.98 mA cm^{-2} at 1.23 V$_{RHE}$ IPCE ~32.2% at 350 nm (1.23 V$_{RHE}$) Stability test for 2 h (decayed ~50%)	[117]
FTO/WO$_3$(002)/m-WO$_3$	Solvothermal/ Spin coating	Nanoparticles	0.1 M Na$_2$SO$_4$	300Xe lamp AM1.5G 100 mW cm^{-2}	1.1 mA cm^{-2} at 1.23 V$_{RHE}$ Stability test for 2 h (decayed ~14%)	[118]

carrier transfer by its unique property of minimization of lattice mismatch. Further PEC enhancement was achieved in the presence of the Bi_2S_3 nanoparticles, which enabled improving carrier separation and transportation and inhibited their recombination due to the band alignment in the $Fe:WO_3/Bi_2S_3$ heterojunction. In terms of photoresponse, the device provided a Δj_{ph} of 2.55 mA cm^{-2} at 1.23 V$_{RHE}$ and stability of 2 h (Δj_{ph} retention of ~90% from its initial value). In short, the homojunction's well-matched staggered alignment band structure allowed electrons and holes to migrate more easily between $Mo:WO_3$ and $Fe:WO_3$ bands and led to better PEC performance.

Ma and co-workers have grown hierarchical layers of WO_3 on tungsten substrate by the one-step aqua-regia hydrothermal method [116]. This approach allowed obtaining homojunction-based WO_3 photoanode with different layer sizes featuring an inner layer of nanoparticles, a middle layer of structured multi-layer, and an outer layer of nanosheet arrays (Fig. 13).

The authors learned from the XPS analyses that the presence of distributed homojunction caused an oxygen vacancy gradient across the layers, namely high and low O_v as shown in Fig. 13(f and g). Such gradient resulted in the formation of a spatially distributed built-in electric field or an enlarged distributed (quasi-) Fermi level gradient which greatly allowed improvement of PEC water splitting. In another study, a new design of homojunction-based WO_3 photoanodes was built to improve the charge separation and transfer for an efficient PEC O_2 evolution. In this case, Li and co-workers proposed a homojunction consisting of 2D nonstoichiometric WO_{3-x} nanoflakes that are vertically grown on 1D WO_3 nanorods [117]. Interestingly, the larger active area of the 2D structure maximized light collection and the 1D structure benefited the charge transfer. Additionally, the homojunction formed between these structures improved the charge separation efficiency.

In these studies presented, several benefits were attributed when employing a homojunction of WO_3, such as high rates of light-harvesting and solar conversion, and improved stability. Although $Mo:WO_3/Fe:WO_3/Bi_2S_3$ and W/WO_3 hierarchical systems presented higher Δj_{ph} values, only the 1D-WO_3/2D-WO_{3-x} photoanode maintained its integrity during stability assessments. Its durability may be associated with the different morphologies obtained from the homojunction and deserves a more in-depth investigation to obtain an even further PEC improvement. A summary of homojunction-based WO_3 photoanodes for PEC O_2 generation is displayed in Table 6.

3.4. Heterojunction-based WO_3 photoanodes

The employment of heterojunctions allows combining different properties of semiconductors to produce unique optoelectronic characteristics that are not available in each semiconductor. These benefits are due to the appropriate combination of the energy band levels of each semiconductor, and it is necessary to have a nearly-matched overlapping band structure [119]. Such an approach can potentially enable improvement in photocatalytic performance due to broadening light-harvesting, minimization of recombination process, improving photogenerated charges separation efficiency, and suppression of photocorrosion process [12,14,120].

Depending on the valence and conduction band positions of a semiconductor compared to another one in a heterostructure, different types of heterostructure can arise such as type II heterostructure [120]. In this configuration, the CB and VB of a given semiconductor are more negative than the respective bands of the other semiconductor. Such band arrays allow the transport of the photogenerated electron and holes in opposite directions, which hinder carriers' recombination and favour PEC water splitting [121]. In terms of semiconductor materials, i.e., WO_3 films, applied in the heterostructure, the $WO_3/BiVO_4$ [122] and $WO_3/$
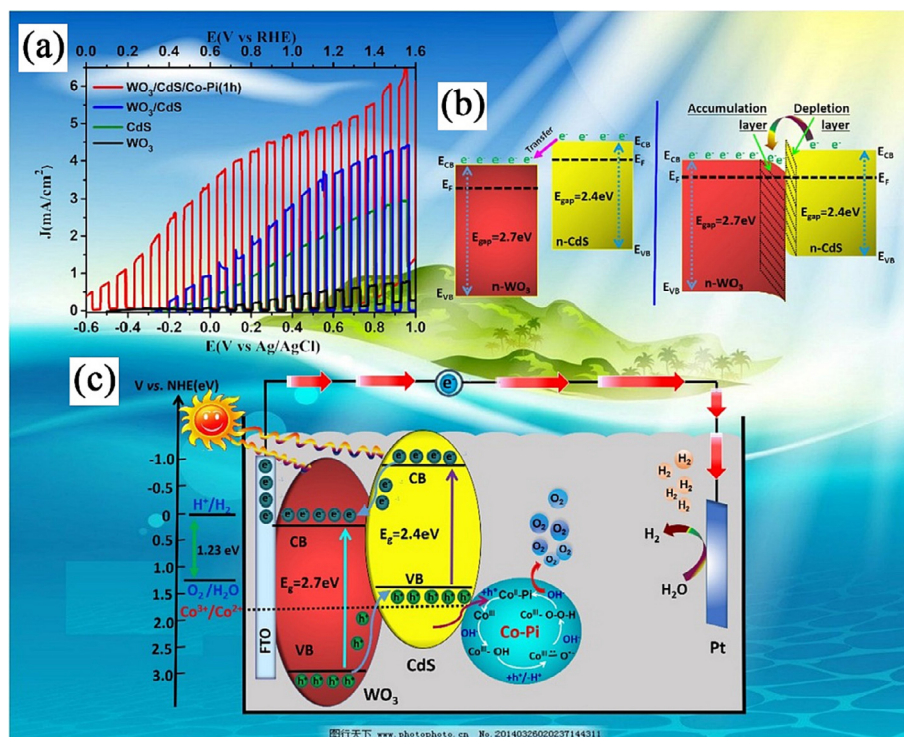
Fe_2O_3 [123] systems are the most widely used for PEC water photoelectrooxidation. In addition to the heterostructure approach, Z-scheme is another strategy highly considered as it has demonstrated to be effective to provide improvement for PEC water splitting. For such a system, the $WO_3/g-C_3N_4$ [124], WO_3/Cu_2O [125], and $BiVO_4/W/WO_3$ [126] have recently emerged as new Z-scheme configurations for an efficient PEC water photoelectrooxidation.

In addition to the presented heterostructure-based WO_3 films, several notable heterojunctions have recently been reported in the literature, mainly the ones consisting of transition metal dichalcogenides (TMD) such as WS_2. This material features having a high catalytic activity which makes it a promising material for water photoelectrooxidation. Employing WS_2, Tayebi and co-workers proposed the manufacture of the WO_3/WS_2 featuring nanosheet structure, which was prepared by liquid-phase exfoliation combined with ultrasonication [127]. The high PEC performance was attributed to the presence of WS_2 nanosheets, being responsible for the increase in light-harvesting, enhanced charge separation and transport, and band alignment. Despite this system delivering a substantial Δj_{ph} of 5.6 mA cm^{-2} at 1.23 V$_{Ag/AgCl}$, photoinstability stood as an issue to be overcome. In another study, Mojaddami and Simchi produced a mixture of WS_2 and MoS_2 which was loaded on W/WO_3 films via cathodic electrophoretic deposition [128]. The prepared system presented a Δj_{ph} of ~1.7 mA cm^{-2} at 1.23 V$_{RHE}$ and a substantial current density of 14.9 mA cm^{-2} at 1.23 V$_{RHE}$, which indicates that the combination of these TMDs can promote a high electrocatalytic activity for OER. Furthermore, the heterostructure remained stable for 2.8 h. Another TMD-based heterostructure comprised of WO_3/VS_2 was obtained by Moi and co-workers [129]. The authors demonstrated that the presence of VS_2 acted as a hole trapping agent of the WO_3 valence band and that it favoured kinetics for OER. Moreover, VS_2 presented active sites on the edge and basal planes for the occurrence of OER [130]. In terms of photoresponse for the OER, the FTO/WO_3/VS_2 film displayed a Δj_{ph} of 2.2 mA cm^{-2} at 1.23 V$_{RHE}$ which was ~5.4 times higher than for the unmodified WO_3 film.

Hosseini and co-workers have investigated the use of organic/inorganic semiconductors based on polyaniline/WO_3 (PANI/WO_3) for PEC water oxidation. In 2019, the authors manufactured camphor sulfonic acid doped polyaniline/WO_3 modified with rGO (CSA:PANI/WO_3/rGO) and obtained an increasing improvement in the photocatalytic activity as each layer was deposited [131]. The rGO incorporation on CSA:PANI/WO_3 promoted improvements in the charge separation and transfer kinetics at the photoelectrode|electrolyte interface, making OER more feasible. Lately, the author has modified the PANI/WO_3 system with the (6,6)-phenyl-C61-butyric acid methyl ester (PC61BM) and achieved higher rates of water photoelectrooxidation [132]. This improvement was assigned to the PC61BM which is a fullerene derivative that enabled better electron accepting capability and electron mobility compared to C60 [132,133]. Employing this type of superficial modification (i.e., PC61BM), provided several benefits to the system, such as high electrical conductivity and carrier mobility, smaller E_g, and larger surface area, which led to an improved Δj_{ph} of 1.63 mA cm^{-2} at 1.23 V$_{RHE}$. In short, organic/inorganic semiconductors have shown promising photoelectrocatalysts features as well as being a noble metal-free alternative for an efficient PEC solar water splitting.

Another interesting heterostructure that deserves attention is the one made up of WO_3/CdS. Recently, two works have been published using WO_3 photoanodes coated with CdS that were obtained by hydrothermal method [134] and successive ionic layer adsorption and reaction [135]. For one of these studies, an additional layer of Co-Pi co-catalyst was deposited over the heterostructure and that enabled achieving a noticeable Δj_{ph} of 5.85 mA cm^{-2} at 1.23

M.B. Costa, Moisés A. de Araújo, Marcos V. de Lima Tinoco et al.

Journal of Energy Chemistry 73 (2022) 88–113

Fig. 14. (a) Linear sweep voltammograms at 20 mV s^{-1} and under chopped solar light simulator for WO$_3$, CdS, WO$_3$/CdS, and WO$_3$/CdS/Co-Pi(1 h) films. The electrolyte was a PBS of 0.5 M Na$_2$SO$_3$ at pH 7. Schematic diagrams for (b) WO$_3$/CdS and (c) WO$_3$/CdS/Co-Pi systems. Reproduced from Ref. [134] with permission from Elsevier, Copyright 2019.

V_{RHE} (cf. Fig. 14a). Most impressive, the optimized condition provided shifting the E_{on} in 529 mV towards less positive values and this was due to the presence of both CdS and mainly Co-Pi. Regarding the stability test, the Δj_{ph} response maintained ~85% of its initial value once elapsed 1.1 h. For the improved photoelectroactivity and stability, the authors reported that was due to the presence of CdS that created a built-in electric field or a (quasi-)Fermi level gradient at the WO$_3$|CdS interface, which provided improving the separation of the photogenerated charges. Despite this improvement in carrier separation, the photogenerated holes tended to accumulate in the CdS valence band, which led to the electron-hole recombination process due to the sluggish OER. Such an issue was overcome by depositing the Co-Pi over the heterostructure which enabled improvement of carriers transfer and consequently enhanced PEC performance for water oxidation (see Fig. 14b and c) [134].

In another study, Li and co-workers added a dual-layer co-catalyst consisting of NiOOH (as hole storage layer) and Co-Pi (as hole transfer layer) on WO$_3$/CdS films [135]. The FTO/WO$_3$/CdS/NiOOH/Co-Pi system displayed a Δj_{ph} of 2.59 mA cm^{-2} at 1 V_{RHE} and stability of 1.9 h (the Δj_{ph} decayed ~8% from its initial value). It is also worth highlighting the study reported by Lin and co-workers about the manufacture of the heterostructure-based WO$_3$/Fe$_2$WO$_6$ by combining hydrothermal and spray pyrolysis processes [136]. The obtained heterojunction provided a wider light absorption range and the presence of a built-in electric field or a (quasi-)Fermi level gradient enabled a more efficient separation and transportation of the minority carriers from the WO$_3$ to the Fe$_2$WO$_6$. Further PEC improvement of this system was achieved by doping the WO$_3$ films with Fe ions and this resulted in increasing the electrical conductivity, charge transport and transfer at the photoelectrode|electrolyte interface, and enhanced charge carrier diffusion and lifetime. The authors also deposited a co-catalyst layer of FeOOH/NiOOH over the Fe:WO$_3$/Fe$_2$WO$_6$ films, which enabled reducing interfacial recombination and accelerating PEC water oxidation reaction. In terms of photoresponse, the combina-

tion of band structure engineering with doping and deposition of suitable OER co-catalysts resulted in a Δj_{ph} of 2.78 mA cm^{-2} at 1.23 V_{RHE} and remarkable stability of 4 h (the Δj_{ph} decayed ~3% from its initial value).

Among all the WO$_3$-based heterostructures mentioned so far, those composed of hematite (Fe$_2$O$_3$) and BiVO$_4$ are among the most widely used and promising photoanodes for PEC water splitting. Hematite has several qualities that make it one of the most promising candidates for photoelectrooxidation of water. In addition to its earth-abundant chemical elements, low cost, and is non-toxic, it has important aspects that can be highlighted, such as adequate optical E_g (1.9–2.2 eV) and high stability in neutral and alkaline media [137]. Despite this, hematite still faces several barriers that make it far from its maximum theoretical conversion efficiency of solar to chemical energy, such as slow water oxidation kinetics, the short hole diffusion length of photogenerated charge carriers, short lifetime and poor mobility of charge carriers [138,139].

Kim and co-workers developed a core-shell structure of an ultrathin layer of Fe$_2$O$_3$ deposited by ALD over mesoporous WO$_3$ grown on FTO (FTO/WO$_3$/Fe$_2$O$_3$) [123]. This heterostructure system allowed shifting the E_{on} towards less positive potential values in comparison with the Fe$_2$O$_3$ and it was assigned to the occurrence of a type II heterostructure and the formation of a strong built-in electric field in the SCR. The mesoporous scaffold structure photoanode also allowed multiple light absorption and reached a Δj_{ph} of 0.83 mA cm^{-2} at 1.23 V_{RHE}, which was higher than the bare Fe$_2$O$_3$ film. Further PEC improvement of this heterostructure was achieved in terms of minimization of charge recombination via deposition of an overlayer of TiO$_2$ and a cobalt phosphate (Co-Pi) co-catalyst layer [140]. When combined all the optimizations to obtain the FTO/WO$_3$/Fe$_2$O$_3$/TiO$_2$/Co-Pi photoanode, the maximum Δj_{ph} was achieved, reaching 1.5 mA cm^{-2} at 1.23 V_{RHE} and 4.1 mA cm^{-2} at 1.7 V_{RHE}. The authors proposed the formation of a type II heterojunction between the WO$_3$ and Fe$_2$O$_3$, which resulted in an improved charge separation due to the strong built-in electric field or the enlarged (quasi-)Fermi level gradient

M.B. Costa, Moisés A. de Araújo, Marcos V. de Lima Tinoco et al.

Journal of Energy Chemistry 73 (2022) 88–113
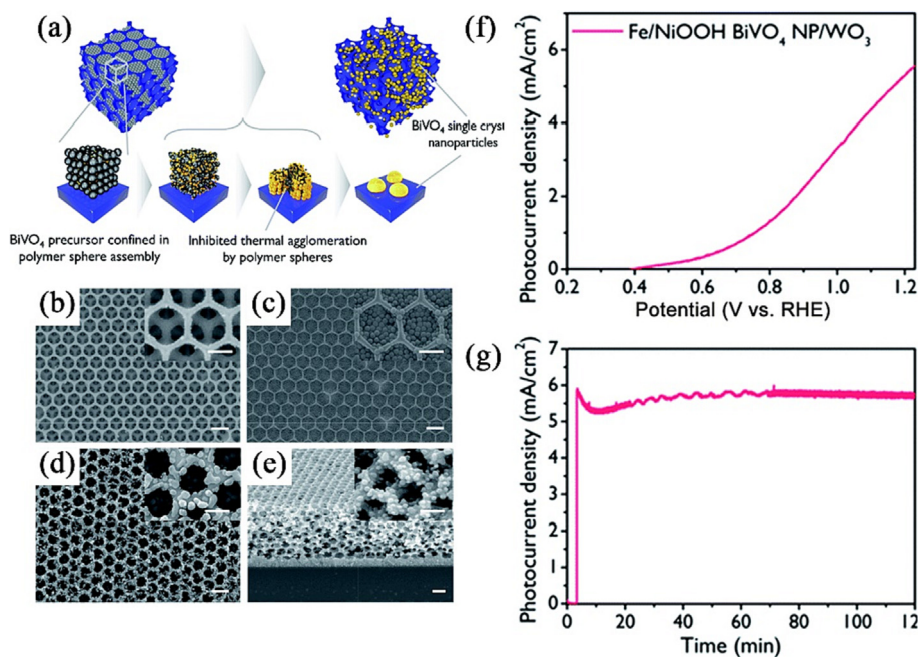
Fig. 15. (a) Schematic representation for the fabrication of the WO$_3$/BiVO$_4$ porous nanostructure. SEM micrographs for the (b) WO$_3$ porous structure, (c) WO$_3$ infiltrated with the polystyrene colloid, (d) WO$_3$/Mo:BiVO$_4$ structure, and (e) cross-sectional SEM image for the WO$_3$/Mo:BiVO$_4$. The scale bars are 1 μm and the insets are their magnified images with scale bars of 0.5 μm. (f) Linear sweep voltammograms under solar light simulator (AM1.5G and 100 mW cm^{-2}) and (g) PEC stability at 1.23 V$_{RHE}$ and under solar light simulator (AM1.5G and 100 mW cm^{-2}) for the WO$_3$/Mo:BiVO$_4$/FeOOH/NiOOH. The electrolyte was a solution of 0.5 M Na$_2$SO$_4$ and 0.1 M Na$_2$SO$_3$ at pH 7. Reproduced (adapted) from Ref. [148] with permission from Royal Society of Chemistry, Copyright 2019.

in the SCR [123,141]. Additionally, the thin TiO$_2$ overlayer introduced a built-in potential that reduced the hole trap in the Fe$_2$O$_3$ surface, while the Co-Pi acted as a hole-transfer co-catalyst which provided a faster hole transfer at the photoanode|electrolyte interface [123].

Wu and co-workers also reported a type II heterojunction made up of WO$_3$/Ti-Fe$_2$O$_3$ in which both materials are n-type semiconductors [140]. The WO$_3$ films were grown by hydrothermal method, which consisted of placing the clean FTO substrates in the vessel containing the precursor solution at 120 ℃ for 2 h. The Ti-Fe$_2$O$_3$ was also deposited over the WO$_3$ nanosheet array via the hydrothermal method with subsequent annealing at 550 ℃. In this work, the authors compared the Δj_{ph} of the Ti-Fe$_2$O$_3$ film deposited on FTO and FTO/WO$_3$. The FTO/WO$_3$/Ti-Fe$_2$O$_3$ photoanode reached a Δj_{ph} of 2.15 mA cm^{-2} at 1.23 V$_{RHE}$, which was ∼4 times higher than the Ti-Fe$_2$O$_3$ deposited over FTO. The heterostructured photoanode also showed great stability, which kept almost constant a Δj_{ph} of 2.5 mA cm^{-2} at 1.23 V$_{RHE}$ for 1.9 h. The WO$_3$/Ti-Fe$_2$O$_3$ heterojunction also displayed an increase of 45% in the photon-to-current efficiency, which was attributed to the improvement of charge separation and charge transfer yields. In addition, the electrochemical impedance spectroscopy results indicated that this heterojunction allowed a faster hole transfer at the photoanode|electrolyte interface.

In another study, Fan and co-workers obtained nanoarrays of WO$_3$ onto FTO substrate by hydrothermal method followed by deposition of the Fe$_2$O$_3$ thin layer by spin coating (FTO/WO$_3$/Fe$_2$O$_3$) [142]. The authors compared the photoelectroactivity of the FTO/WO$_3$/Fe$_2$O$_3$ with the individual materials and studied the optimal load of Fe$_2$O$_3$ varying the spin coating by 10, 20, and 50 times. The optimized FTO/WO$_3$/Fe$_2$O$_3$ photoanodes (spin-coated Fe$_2$O$_3$ for 20 times) showed by the PEC experiments that the formation of the core-shell heterojunction not only improved the Δj_{ph}, reaching 1.29 mA cm^{-2} at 1.23 V$_{RHE}$, but also resulted in shifting the E_{on} in 210 mV towards less positive values. Despite these improvements, the Δj_{ph} of the FTO/WO$_3$/Fe$_2$O$_3$ at the lower poten-

tial region was slightly lower than the bare WO$_3$, which was attributed to a large number of surface states in the Fe$_2$O$_3$. To overcome this issue was deposited a co-catalyst comprised of NiFe-layered double hydroxide (NiFe-LDH), which contributed to shifting the E_{on} in 50 mV to less positive values and substantially increase of the Δj_{ph} at relative lower potentials. The FTO/WO$_3$/Fe$_2$O$_3$ and FTO/WO$_3$/Fe$_2$O$_3$/NiFe-(LDH) also presented great stability, maintaining 73% and 94.5% of their Δj_{ph} for 1 h, respectively.

Concerning the WO$_3$/BiVO$_4$ heterostructure, BiVO$_4$ is an n-type semiconductor with a narrow direct optical E_g of ∼2.4 eV for its monoclinic phase, which is ideal for absorbing photons in the visible range of the solar spectrum. BiVO$_4$ has also shown excellent results, such as featuring STH exceeding 4% in devices based on dual-photoelectrodes only assisted by solar light [143]. Additionally, the CB and VB positions of this material are suitably positioned to construct a type-II heterostructure with WO$_3$ [144]. Since BiVO$_4$ has poor charge separation, the combination of its optoelectronic properties with those of WO$_3$ can potentially overcome this issue by enabling rapid charge separation at the heterojunction interface [144–146]. This makes WO$_3$/BiVO$_4$ heterojunction one of the most explored systems in the literature [147].

One of the highest Δj_{ph} results obtained so far for the WO$_3$/BiVO$_4$ system was achieved by Kim and co-workers, which employed a WO$_3$ scaffold coated with nanoparticles of Mo:BiVO$_4$ (cf. Fig. 15a–e) [148]. The scaffold was obtained via drop-casting of WO$_3$ precursor solution onto colloidal crystal-coated FTO substrate [148]. Subsequently, the authors photoelectrodeposited a dual-layer of FeOOH/NiOOH over the FTO/WO$_3$/Mo:BiVO$_4$ films. This system delivered a substantial Δj_{ph} of 5.8 mA cm^{-2} at 1.23 V$_{RHE}$ for water oxidation and was stable for 2 h, as shown in Fig. 15(f and g), respectively. The results also indicated that charge transport occurs more efficiently in BiVO$_4$ nanoparticles than in a continuous shell. Furthermore, the light absorption efficiency of the system was improved due to the nanoparticles of BiVO$_4$ that enhanced Rayleigh-type light scattering, mainly at the absorption edge wavelengths.

Table 7
Summary of heterojunction-based WO_3 photoanodes for PEC water splitting application.

Material	WO_3 fabrication method	WO_3 morphology	Electrolyte	Illumination	Notable PEC results	Ref.
$W/WO_3/WS_2$	Sonochemically assisted method	Nanoplates	0.5 M Na_2SO_4	300 W Xe lamp AM1.5G 100 mW cm^{-2}	5.6 mA cm^{-2} at 1.23 $V_{Ag/AgCl}$ IPCE 55.2% at 350 nm (0.6 $V_{Ag/AgCl}$) ABPE 2.26% at 0.75 $V_{Ag/AgCl}$	[127]
$W/WO_3/WS_2$-MoS_2	Hydrothermal	Nanoflakes	0.5 M H_2SO_4	350 W Xe lamp 100 mW cm^{-2}	~1.7 mA cm^{-2} at 1.23 V_{RHE} Stability test for 2.8 h (approx. const.)	[128]
$FTO/WO_3/VS_2$	Hydrothermal	Nanoflakes	0.1 M Na_2SO_4	300 W W lamp 100 mW cm^{-2}	2.2 mA cm^{-2} at 1.23 V_{RHE} IPCE 23% at 350 nm	[129]
$FTO/WO_3/In_2S_3$	Hydrothermal	Nanowalls	0.1 M Na_2SO_4	Xe lamp AM1.5G 100 mW cm^{-2}	1.61 mA cm^{-2} at 1.23 V_{RHE} E_{on} = 0.02 V_{RHE} ABPE 0.29% at 0.88 V_{RHE}	[153]
$FTO/WO_3/CdIn_2S_4$	Hydrothermal	Nanowalls	0.25 M Na_2SO_4	AM1.5G 100 mW cm^{-2}	1.06 mA cm^{-2} at 1.23 V_{RHE} E_{on} = 0.14 V_{RHE} IPCE 41.5% at 360 nm (1.23 V_{RHE})	[154]
$FTO/WO_3/ZnIn_2S_4/AESI^a$ (^{a}AESI: N-(2-aminoethyl)-3-aminopropyltrim-ethoxysilane)	Hydrothermal	Nanosheets	0.5 M Na_2SO_4	AM1.5G 100 mW cm^{-2}	1.51 mA cm^{-2} at 1.23 V_{RHE} E_{on} = 0.4 V_{RHE} IPCE 50.6% at 365 nm (1.23 V_{RHE}) ABPE 0.19% at ~0.95 V_{RHE} Stability test for 1 h (decayed ~50%)	[155]
ITO/CSA:PANI-WO_3/rGO	WO_3 nanoparticules/spin coating	Pellet-like nanoparticles	0.1 M Na_2SO_4	300 W Xe lamp 100 mW cm^{-2}	1.54 mA cm^{-2} at 1.23 V_{RHE} ABPE 0.29% at ~0.85 V_{RHE}	[131]
ITO/PANI-WO_3/PC61BM	WO_3 nanoparticules/spin coating	Nanoparticles	0.1 M Na_2SO_4	300 W Xe lamp 100 mW cm^{-2}	1.63 mA cm^{-2} at 1.23 V_{RHE}	[132]
$FTO/CuWO_4/WO_3$	Hydrothermal	Urchin-like	0.2 M PBS pH 7	300 W Xe lamp AM1.5G	0.48 mA cm^{-2} at 1.23 V_{RHE} E_{on} = 0.6 V_{RHE} Stability test for 3 h (decayed ~20%)	[156]
$FTO/WO_3/CuWO_4$/Co-Pi	Hydrothermal	Nanoplates	0.2 M Na_2SO_4	AM1.5G 100 mW cm^{-2}	1.4 mA cm^{-2} at 1.23 V_{RHE} ABPE 0.55% at ~0.70 V_{RHE} Stability test for 2 h (decayed ~10%)	[157]
FTO/WO_3/rocksalt-CoO_x	Hydrothermal	Nanoplates	0.5 M Na_2SO_4	300 W Xe lamp AM1.5G 100 mW cm^{-2}	0.53 mA cm^{-2} at 1.23 V_{RHE} IPCE 23.5% at 350 nm ABPE 0.062% at 1.03 V_{RHE}	[158]
$FTO/WO_3/CdS$/Co-Pi	Hydrothermal	Plates	0.1 PBS + 0.5 M Na_2SO_3	300 W Xe lamp AM1.5G 100 mW cm^{-2}	5.85 mA cm^{-2} at 1.23 V_{RHE} IPCE 41.8% at 420 nm (1.23 V_{RHE}) ABPE 1.80% at 0.7 V_{RHE} Stability test for 1.1 h (decayed ~15%)	[134]
$FTO/WO_3/CdS/NiOOH$/Co-Pi	Hydrothermal	Nanorods	0.2 M Na_2SO_4	AM1.5G 100 mW cm^{-2}	2.59 mA cm^{-2} at 1 V_{RHE} LHE 90% at 300–450 nm ABPE 1.02% at 0.64 V_{RHE} E_{on} ≈ 0.3 V_{RHE} Stability test for 1.9 h (decayed ~8%)	[135]
$FTO/WO_3/Bi_2O_2NCN$	Hydrothermal	Not informed	0.1 M potassium phosphate (KP$_i$)	450 W Xe lamp AM1.5G 100 mW cm^{-2}	1.11 mA cm^{-2} at 1.23 V_{RHE} IPCE ~10.5% at 380 nm (1.23 V_{RHE}) Stability test for ~0.33 h (decayed ~25%)	[159]
$FTO/WO_3/NiCo_2O_4$	Hydrothermal	Nanoplates	0.2 M Na_2SO_4	AM1.5G 100 mW cm^{-2}	0.84 mA cm^{-2} at 1.23 V_{RHE} Stability test for 2 h (decayed ~10%)	[160]
$FTO/WO_3/Ni(OH)_2$	Hydrothermal	Blocks and sheets	0.5 M Na_2SO_4	300 W Xe lamp AM1.5G 100 mW cm^{-2}	1 mA cm^{-2} at 0.8 V_{RHE} E_{on} = 0.3 V_{RHE}	[161]
$FTO/Fe:WO_3/Fe_2WO_6/FeOOH/NiOOH$	Hydrothermal	Nanosheets	0.5 M PBS pH 7	450 W Xe lamp AM1.5G 100 mW cm^{-2}	2.78 mA cm^{-2} at 1.23 V_{RHE} ABPE 0.72% at 0.8 V_{RHE} Stability test for 4 h (approx. const.)	[136]

Table 7 (*continued*)

Material	WO$_3$ fabrication method	WO$_3$ morphology	Electrolyte	Illumination	Notable PEC results	Ref.
FTO/WO$_3$/rGO/Ni:FeOOH	Hydrothermal	Nanoflakes	0.5 M Na$_2$SO$_4$	Xe lamp 100 mW cm^{-2}	1.32 mA cm^{-2} at 1.23 V$_{RHE}$ IPCE 96.% at 380 nm Stability test for 6 h (decayed ~5%)	[162]
FTO/WO$_3$/CQDs/NiFe	Solvothermal	Nanoflakes	0.2 M Na$_2$SO$_4$	300 W Xe lamp AM1.5G 100 mW cm^{-2}	1.43 mA cm^{-2} at 1.23 V$_{RHE}$ IPCE 38.6% at 405 nm (1.23 V$_{RHE}$) ABPE 0.16% at 1 V$_{RHE}$ Stability test for 3 h (approx. const)	[163]
FTO/WO$_3$/α-Fe$_2$O$_3$/TiO$_2$/Co-Pi	Drop-casting/sol–gel	Mesoporous/nanoparticles	1 M NaOH	AM1.5G 100 mW cm^{-2}	1.5 mA cm^{-2} at 1.23 V$_{RHE}$ IPCE ~17.5% at 300–400 nm (1.23 V$_{RHE}$) Stability test for 1.7 h (decayed ~10%)	[123]
FTO/WO$_3$/Fe$_2$O$_3$	Hydrothermal	Cuboid sheets	1 M NaOH	AM1.5G 100 mW cm^{-2}	0.78 mA cm^{-2} at 0.8 V$_{Ag/AgCl}$ Stability test for 0.28 h (decayed ~70%)	[164]
FTO/WO$_3$/Ti-Fe$_2$O$_3$	Hydrothermal	Nanosheets	1 M KOH	300 W Xe lamp AM1.5G 100 mW cm^{-2}	2.15 mA cm^{-2} at 1.23 V$_{RHE}$ IPCE ~60% at 370 nm (1.23 V$_{RHE}$) E_{on} = 0.92 V$_{RHE}$ Stability test for 1.95 h (decayed ~20%)	[140]
FTO/WO$_3$/Fe$_2$O$_3$/NiFe-LDH	Hydrothermal	Nanorods	Not imformed	150 W Xe lamp AM1.5G	1.29 mA cm^{-2} at 1.23 V$_{RHE}$ E_{on} = 0.65 V$_{RHE}$ IPCE 26% at 350 nm (1.23 V$_{RHE}$) ABPE 0.268% at 0.91 V$_{RHE}$ Stability test for 1 h (decayed 5.5%)	[142]
FTO/WO$_3$/Fe$_2$O$_3$/Co(OH)$_x$	Electrospray	Irregular porous skeleton morphology	1 M NaOH	450 W Xe lamp AM1.5G 100 mW cm^{-2}	0.62 mA cm^{-2} at 1.23 V$_{RHE}$ IPCE 19% at 350 nm (1.23 V$_{RHE}$) Stability test for 1 h (decayed ~33%)	[137]
FTO/WO$_3$/Fe$_2$O$_3$/FeOOH	Hydrothermal	Nanorods	0.2 M Na$_2$SO$_4$	Xe lamp AM1.5G 100 mW cm^{-2}	1.12 mA cm^{-2} at 1.23 V$_{RHE}$ E_{on} ≈ 0.3 V$_{RHE}$ ABPE 0.32% at 0.65 V$_{RHE}$ Stability test for 2 h (approx. const)	[165]
FTO/WO$_3$/BiVO$_4$	Hydrothermal	Nanorods	0.5 M KH$_2$PO$_4$	500 W Xe lamp 100 mW cm^{-2}	1.56 mA cm^{-2} at 1.23 V$_{RHE}$ E_{on} ≈ 0.4 V$_{RHE}$ IPCE ~40% at 350 nm (1.23 V$_{RHE}$) Stability test for 2 h (decayed 10%)	[122]
FTO/WO$_3$/BiVO$_4$/Co-Pi	Spin coating	Nanoplates	0.1 M KPi	500 W Xe lamp AM1.5G 100 mW cm^{-2}	1.8 mA cm^{-2} at 1.23 V$_{RHE}$ IPCE ~60% at 360 nm (1.23 V$_{RHE}$) ABPE 0.6% at 0.75 V$_{RHE}$ Stability test for 0.33 h (decayed ~30%)	[166]
FTO/WO$_3$/BiVO$_4$/ZnO	Hydrothermal	Nanoplates	0.5 M Na$_2$SO$_4$	300 W Xe lamp AM1.5G 100 mW cm^{-2}	2.96 mA cm^{-2} at 1.23 V$_{RHE}$ E_{on} = 0.3 V$_{RHE}$ IPCE ~72.8% at 380 nm (1.23 V$_{RHE}$) Stability test for 6 h (decayed 9%)	[147]
FTO/WO$_3$/BiVO$_4$	Hydrothermal	Blocks	0.5 M KPi pH≈7.2	150 W Xe lamp AM1.5G 100 mW cm^{-2}	High Δj_{ph} between 0.8–1.2 V$_{RHE}$ E_{on} = 0.868 V$_{RHE}$ IPCE ~37% at 440 nm	[167]
FTO/WO$_3$/Mo:BiVO$_4$/NiOOH/FeOOH	Drop-casting	Porous structure	0.5 M Na$_2$SO$_4$ + 0.1 M Na$_2$SO$_3$	AM1.5G 100 mW cm^{-2}	5.8 mA cm^{-2} at 1.23 V$_{RHE}$ IPCE ~95% at 400–450 nm (1.23 V$_{RHE}$) Stability test for 2 h (decayed 3%)	[148]
FTO/WO$_3$/BiVO$_4$/BiFeO$_3$	Sol-gel	Planar surface	0.5 M Na$_2$SO$_4$	Xe lamp AM1.5G 100 mW cm^{-2}	46.9 mA cm^{-2} at 2.53 V$_{RHE}$ E_{on} = 0.5 V$_{RHE}$ Stability test for 0.83 h (decayed 30%)	[168]
SLG/SnO$_2$/WO$_3$/BiVO$_4$	Electrodeposition	Not informed	0.1 M Na$_2$SO$_4$	Xe lamp 100 mW cm^{-2}	~0.7 mA cm^{-2} at 0.8 V$_{Ag/AgCl}$ EQE ~70% at ~250–300 nm (0.8 V$_{Ag/AgCl}$)	[169]
FTO/WO$_3$/BiVO$_4$/NiTCPP	Spin coating	Nanostructures	0.1 M Na$_2$SO$_4$	500 W Xe lamp AM1.5G 100 mW cm^{-2}	0.26 mA cm^{-2} at 0.6 V$_{RHE}$ ABPE 0.25% at 0.82 V$_{RHE}$ Stability test for 0.25 h (decayed > 50%)	[170]

Table 7 (continued)

Material	WO$_3$ fabrication method	WO$_3$ morphology	Electrolyte	Illumination	Notable PEC results	Ref.
FTO/WO$_3$/BiVO$_4$	Spin coating	Not informed	0.5 M Na$_2$SO$_4$	AM1.5G 100 mW cm^{-2}	~0.6 mA cm^{-2} at 1.23 V$_{RHE}$ IQE ~24% at 360 nm (1.23 V$_{RHE}$)	[171]
FTO/WO$_3$/BiVO$_4$	Hydrothermal	Nanorods	0.5 M KPi pH 7 + 0.1 M Na$_2$SO$_3$	AM1.5G 100 mW cm^{-2}	4.15 mA cm^{-2} at 1.23 V$_{RHE}$ IPCE 75.9% at 430 nm (1.23 V$_{RHE}$) Stability test for 7.8 h (approx. const.)	[149]
FTO/WO$_3$/BiVO$_4$	Hydrothermal	Nanorods	0.5 M KPi pH 7.3 + 1 M Na$_2$SO$_3$	Xe lamp AM1.5G 100 mW cm^{-2}	3.87 mA cm^{-2} at 1.23 V$_{RHE}$ IPCE ~70% at 400–500 nm Stability test for 6.95 h for 24 days (approx. const.)	[150]
FTO/TiO$_2$/WO$_3$/BiVO$_4$/(FiOOH/NiOOH)	Electrodeposition	brochosomes-like	0.5 M Na$_2$SO$_4$	AM1.5G 100 mW cm^{-2}	~2.47 mA cm^{-2} at 1.23 V$_{RHE}$ IPCE 60.1% at 430 nm (1.23 V$_{RHE}$) Stability test for 5 h (decayed ~20%)	[172]
FTO/WO$_3$/BiVO$_4$	Hydrothermal	Nanoplates	0.5 M Na$_2$SO$_4$	AM1.5G 100 mW cm^{-2}	1.7 mA cm^{-2} at 1.23 V$_{RHE}$ IPCE 33.8% at 410 nm (1.23 V$_{RHE}$) E_{on} = 0.15 V$_{RHE}$ Stability test for 2 h (decayed ~2%)	[173]
W/WO$_3$/BiVO$_4$/CoO$_x$	Hydrothermal	Not informed	0.2 M Na$_2$SO$_4$	300 W Xe lamp AM1.5G ~80 mW cm^{-2}	2.3 mA cm^{-2} at 0.8 V$_{RHE}$ IPCE ~41% at 400 nm (1.23 V$_{RHE}$) Stability test for 0.17 h	[174]
FTO/WO$_3$/BiVO$_4$	Hydrothermal	Nanoflakes	0.5 M PBS pH 7.2	AM1.5G 100 mW cm^{-2}	1.5 mA cm^{-2} at 1.23 V$_{RHE}$ IPCE ~50% at 300–400 nm (0.61 V$_{Ag/AgCl}$)	[175]
FTO/WO$_3$/BiVO$_4$	Spin coating	Worm-like	0.5 M Na$_2$SO$_4$	100 W LED	0.187 mA cm^{-2} at 1.23 V$_{RHE}$ ABPE ~1% at ~0.7 V$_{RHE}$	[176]
FTO/WO$_3$-1D/BiVO$_4$/Co-Pi	Flame vapour deposition	Nanowires	0.1 M KP$_i$	300 W Xe lamp AM1.5G 100 mW cm^{-2}	3.3 mA cm^{-2} at 1.23 V$_{RHE}$ E_{on} ≈ 0.45 V$_{RHE}$ IPCE 50% at 420 nm (1 V$_{SCE}$) ABPE 0.7% at 0.88 V$_{RHE}$	[144]
FTO/WO$_3$/BiVO$_4$/TANiFe	Hydrothermal	Nanoplates	0.5 M borate Buffer pH 8.5	300 W Xe lamp AM1.5G 100 mW cm^{-2}	3.7 mA cm^{-2} at 1.23 V$_{RHE}$ IPCE 69.4% at 420 nm (1.23 V$_{RHE}$) ABPE 0.95% at 0.76 V$_{RHE}$ Stability test for 5 h (decayed ~15%)	[177]
FTO/(W$_{x-0.05}$Mo$_x$)O$_3$–(Sn$_{x-0.05}$Nb$_x$)O$_2$:N	Hydrothermal	Nanotubes	1.0 M H$_2$SO$_4$	Xe lamp AM1.5G 100 mW cm^{-2}	4.13 mA cm^{-2} at 0.1 V$_{RHE}$ ABPE ~8% at 0.4 V STH 3.12% Stability test for 24 h (decayed ~5%)	[178]
FTO/BiVO$_4$-NLs/WO$_3$-NRs	Hydrothermal	Nanorods	1.0 M Na$_2$SO$_3$ + 0.5 M PBS pH 7.3	AM1.5G 100 mW cm^{-2}	2.83 mA cm^{-2} at 1.23 V$_{RHE}$ IPCE ~45% at 310–460 nm (1.23 V$_{RHE}$)	[179]
FTO/WO$_3$/BiVO$_4$/NiFeCr	Sputtering	Nanoparticles	0.1 M PBS pH 6.9	AM1.5G 100 mW cm^{-2}	4.9 mA cm^{-2} at 1.23 V$_{RHE}$ IPCE ~56% at 350–470 nm (1.23 V$_{RHE}$) ABPE 0.95% at 0.85 V$_{RHE}$ Stability test for 6 h (decayed ~7%)	[180]
FTO/WO$_3$/BiVO$_4$/ZnO	Spin coating	Planar surface	0.5 M Na$_2$SO$_4$	Xe lamp AM1.5G 100 mW cm^{-2}	0.19 mA cm^{-2} at 1.23 V$_{RHE}$ ABPE 0.036% at 0.41 V$_{RHE}$ IPCE ~6% at 380 nm at 1.23 V$_{RHE}$ Stability test for 0.4 h (decayed ~30%)	[181]
FTO/WO$_3$/Bi$_2$MoO$_6$/Co-Pi	Hydrothermal	Nanoplates	0.5 M Na$_2$SO$_4$	Xe lamp AM1.5G 100 mW cm^{-2}	1.4 mA cm^{-2} at 1.0 V$_{Ag/AgCl}$ IPCE ~67% at 380 nm ABPE 0.07% at 1.06 V$_{RHE}$ Stability test for 3 h (decayed ~4%)	[182]
FTO/WO$_3$/BiVO$_4$/TiO$_2$	Hydrothermal	Nanoplates	0.5 M Na$_2$SO$_4$	Xe lamp AM1.5G 100 mW cm^{-2}	1.04 mA cm^{-2} at 1.23 V$_{RHE}$ IPCE ~25% at 460 nm at 1.23 V$_{RHE}$ Stability test for 24 h (aprox. const.)	[183]
FTO/WO$_3$/BiVO$_4$	Sol-gel	Grains and coating-like	0.1 M KH$_2$PO$_4$	AM1.5G 100 mW cm^{-2}	~2.50 mA cm^{-2} at 1.23 V$_{RHE}$ IPCE ~55% at 400 nm at 1.23 V$_{RHE}$ Stability test for ~6 h (decayed ~60%)	[184]

Table 7 (*continued*)

Material	WO$_3$ fabrication method	WO$_3$ morphology	Electrolyte	Illumination	Notable PEC results	Ref.
FTO/WO$_3$/ZnWO$_4$	Hydrothermal	Nanorods	0.5 M Na$_2$SO$_4$	Xe lamp AM1.5G 100 mW cm^{-2}	2.53 mA cm^{-2} at 1.23 V$_{RHE}$ IPCE ~48% at 465 nm Stability test for ~0.11 h (approx. const.)	[185]
WO$_3$/CuO	Hydrothermal	Nanoparticles	0.5 M Na$_2$SO$_4$	AM1.5G 100 mW cm^{-2}	3.2 mA cm^{-2} at 1.23 V$_{RHE}$ Stability test for 50 h (decayed ~12%)	[186]
FTO/WO$_3$/BiVO$_4$	Spray coating	Compact film	0.1 M Na$_2$HPO$_4$ + 0.5 M Na$_2$SO$_4$	100 W Xe lamp AM1.5G 100 mW cm^{-2}	2.1 mA cm^{-2} at 1.23 V$_{RHE}$ Stability test for 2 h (decayed 46%)	[151]
FTO/WO$_3$/BiVO$_4$	Sputtering using the GLAD	Nanorods	0.5 M Na$_2$SO$_4$ pH 7	AM1.5G 100 mW cm^{-2}	2.24 mA cm^{-2} at 1 V$_{Ag/AgCl}$ E_{on} = 0.42 V$_{Ag/AgCl}$	[187]
FTO/WO$_3$/WS$_2$	Hydrothermal	Nanorods	0.3 M KH$_2$PO$_4$	150 W Xe lamp AM1.5G 100 mW cm^{-2}	~0.5 mA cm^{-2} at ~1.2 V$_{RHE}$	[188]
FTO/WO$_3$/CdS	Hydrothermal	Not informed	0.2 M Na$_2$SO$_4$ pH 0.69	500 W Xe lamp AM1.5G 100 mW cm^{-2}	2.13 mA cm^{-2} at 1.23 V$_{RHE}$ ABPE 0.74% at 0.39 V$_{RHE}$ Stability test for 0.083 h	[189]
FTO/WO$_3$/TiO$_2$/CQDs	Hydrothermal	Nanoplates	0.2 M Na$_2$SO$_4$	300 W Xe lamp AM1.5G 100 mW cm^{-2}	2.03 mA cm^{-2} at 1.23 V$_{RHE}$ ABPE 0.33% at ~0.9 V$_{RHE}$ IPCE ~62.3% at 340 nm (1.23 V$_{RHE}$) Stability test for 5.6 h (decayed 51.8%)	[190]
FTO/WO$_3$/prussian blue	Hydrothermal	Nanorods	0.1 M Na$_2$SO$_4$ pH 7	300 W Xe lamp	0.34 mA cm^{-2} at 1.23 V$_{RHE}$ IPCE 18% at 350 nm (1.23 V$_{RHE}$) Stability test for ~1.4 h (decayed ~9%)	[191]
FTO/WO$_3$/BiVO$_4$/Fe$_2$O$_3$	PLD	Not informed	0.5 M Na$_2$SO$_4$ + 0.5 M Na$_2$SO$_3$	AM1.5G 100 mW cm^{-2}	~2.8 mA cm^{-2} at 1.23 V$_{RHE}$ E_{on} = ~0.3 V$_{RHE}$ IPCE ~10.5% at 350 nm (0.6 V$_{RHE}$) Stability test for 16 h (aprox. const.)	[192]
FTO/WO$_3$/Yb-Mo-BiVO$_4$	Drop-cast	Irregular rod-shaped	1 M K$_2$HPO$_4$ pH 8.7	150 W Xe lamp 130 mW cm^{-2}	1.67 mA cm^{-2} at 0.85 V$_{SCE}$ ABPE 0.81% at 0.85 V$_{SCE}$ Stability test for 1 h (aprox. const.)	[193]
WO$_3$/S:Bi$_2$O$_3$/(Ga,W): BiVO$_4$/Co-Pi	Spray coating	Nanopores	0.1 M KPi	Xe lamp AM1.5G 100 mW cm^{-2}	5.1 mA cm^{-2} at 1.23 V$_{RHE}$ IPCE ~72% at 460 nm (1.23 V$_{RHE}$) Stability test for 10 h (decayed ~10%)	[194]
Ti/WO$_3$/Mo:BiVO$_4$	Spin coating	Nanoparticles	0.1 M H$_2$SO$_4$	300 W Xe lamp 39.5 mW cm^{-2}	2.5 mA cm^{-2} at 1.23 V$_{RHE}$ IPCE ~20% at 300–400 nm (1.23 V$_{RHE}$) Stability test for 2 h (decayed ~50%)	[195]
FTO/WO$_3$/NiFe-LDH	Hydrothermal/ Electrodeposition	Nanoparticles	0.1 M Na$_2$SO$_4$ + 0.1 M KPi	Xe lamp AM1.5G 100 mW cm^{-2}	2.5 mA cm^{-2} at 1.23 V$_{RHE}$ ABPE 0.26% at 0.97 V$_{RHE}$ Stability test for 3.5 h (approx. const.)	[196]
ITO/WO$_3$/Cu$_2$O/CuO	Hydrothermal/ Electrodeposition	Cubic grains	0.5 M Na$_2$SO$_4$	300 W Xe lamp AM1.5G 100 mW cm^{-2}	4.7 mA cm^{-2} at 1.23 V$_{RHE}$ Stability test for 3 h (decayed ~21%)	[197]
FTO/WO$_3$/BiFeO$_3$	Hydrothermal/Spin coating	Nanoplates	0.1 M Na$_2$SO$_4$	300Xe lamp AM1.5G 100 mW cm^{-2}	2.8 mA cm^{-2} at 0.6 V$_{Ag/AgCl}$ Stability test for 0.1 h (decayed ~10%)	[198]
W/WO$_3$/BiVO$_4$/Co-Pi	Hydrothermal	Nanoflakes	0.1 M Na$_2$SO$_4$ + 0.1 M KPi	500Xe lamp AM1.5G 100 mW cm^{-2}	2.3 mA cm^{-2} at 1.23 V$_{RHE}$ ABPE 0.38% at 0.88 V$_{RHE}$ Stability test for 10 h (decayed ~9%)	[199]

M.B. Costa, Moisés A. de Araújo, Marcos V. de Lima Tinoco et al.

Journal of Energy Chemistry 73 (2022) 88–113

Lee and co-workers manufactured $WO_3/BiVO_4$ core-shell nanorod arrays via an all-solution-processed methodology [149]. The vertically aligned WO_3 nanorods were obtained on a FTO substrate by the hydrothermal method without the presence of a seed layer and $BiVO_4$ was deposited by pulsed electrodeposition at 80 °C. Regarding the PEC assessment of this system, it was performed employing sodium sulfite (Na_2SO_3) in the electrolyte solution as a hole scavenger because its oxidation is thermodynamically and kinetically more favourable than the oxidation of water, which allows comparison of the Δj_{ph} obtained from the oxidation of water without the kinetic impediments [145,149]. Increasing the WO_3 hydrothermal synthesis temperature from 120 to 170 °C, the authors noted that the Δj_{ph} increased up to 1.97 mA cm^{-2} at 1.23 V_{RHE} due to enlargement of the nanorods of WO_3, suggesting an increase in active sites on the nanorods. However, the Δj_{ph} decreased to 1.58 mA cm^{-2} at 1.23 V_{RHE} at higher synthesis temperatures (180 °C), and it was assigned to the occurrence of WO_3 bulky rods grown between small nanorods that blocked light and prevented the small nanorods from producing photogenerated charge carriers. The number of deposition cycles of $BiVO_4$ layer onto WO_3 films was systematically evaluated and 9 cycles were found to be the optimized condition. Deposition cycles above 9 resulted in diminished Δj_{ph} due to the increase in the thickness of the $BiVO_4$ film and its short diffusion length, which led to increased recombination of electron-hole pairs. In terms of photoresponse, the optimized $WO_3/BiVO_4$ photoanode reached a Δj_{ph} of 4.15 mA cm^{-2} at 1.23 V_{RHE} in 0.5 M phosphate buffer solution (PBS) pH 7 with 1 M Na_2SO_3. Concerning the stability test, the Δj_{ph} of the bare pristine WO_3 decreased constantly from the beginning of the test, and the WO_3 nanorod array was peeled off after 4 h of measurement. On the other hand, the optimized $WO_3/BiVO_4$ system remained stable for 8 h of the experiment. This implies that without the presence of a seed layer, WO_3 was weakly adhered to the FTO surface, whereas $BiVO_4$ covered the entire surface of

the WO_3 film in a core-shell structure and behaved like a passivation layer.

Employing a similar synthesis approach, Kim and co-workers also obtained $WO_3/BiVO_4$ system, which particularly differed compared to the study above regarding using a WO_3 seed layer deposited on FTO substrate followed by growth of WO_3 nanorods by hydrothermal method [150]. A second step of the hydrothermal treatment allowed the growth of branches on WO_3 nanorods using the same precursor reagents. The authors achieved excellent long-term stability of the system by monitoring the Δj_{ph} for 6.9 h at 1.23 V_{RHE}. The experiment was also monitored for 24 days and showed no significant degradation, meaning the branched WO_3 NR/$BiVO_4$ system is greatly stable for PEC performance.

Employing a different synthesis route, Coelho and co-workers electrodeposited a Bi layer on WO_3 films (obtained by spray coating using an airbrush) and that was subsequently converted to the $BiVO_4$ by the drop-casting addition of NH_4VO_3 and heat treatment [151]. The number of layers of WO_3 spray deposition was studied, as well as the electrodeposition of Bi. In the first case, increasing the number of layers allowed higher Δj_{ph} to be reached for bare WO_3, however, the same was not observed for the $WO_3/BiVO_4$ heterojunction, which lost its photoelectrocatalytic performance. After reaching an optimized WO_3 condition, the electrodeposition of metallic Bi as a precursor of $BiVO_4$ proved to be the best strategy compared to other methodologies of obtaining the heterostructure, such as spin coating and drop-casting. To complete the synthesis, the pulsed Bi electrodeposition ensured a better performance of the heterostructure than that performed continuously with the same deposition charge. In terms of photoresponse for OER, the FTO/$WO_3/BiVO_4$ reached a Δj_{ph} of 2.1 mA cm^{-2} at 1.23 V_{RHE}. Regarding the charge transfer dynamics for $WO_3/BiVO_4$, further understanding of this phenomenon in the $WO_3/BiVO_4$ system has been achieved by the transient absorption (TA) mid-infrared (mid-IR) spectroscopy in the picosecond to microsecond time scale
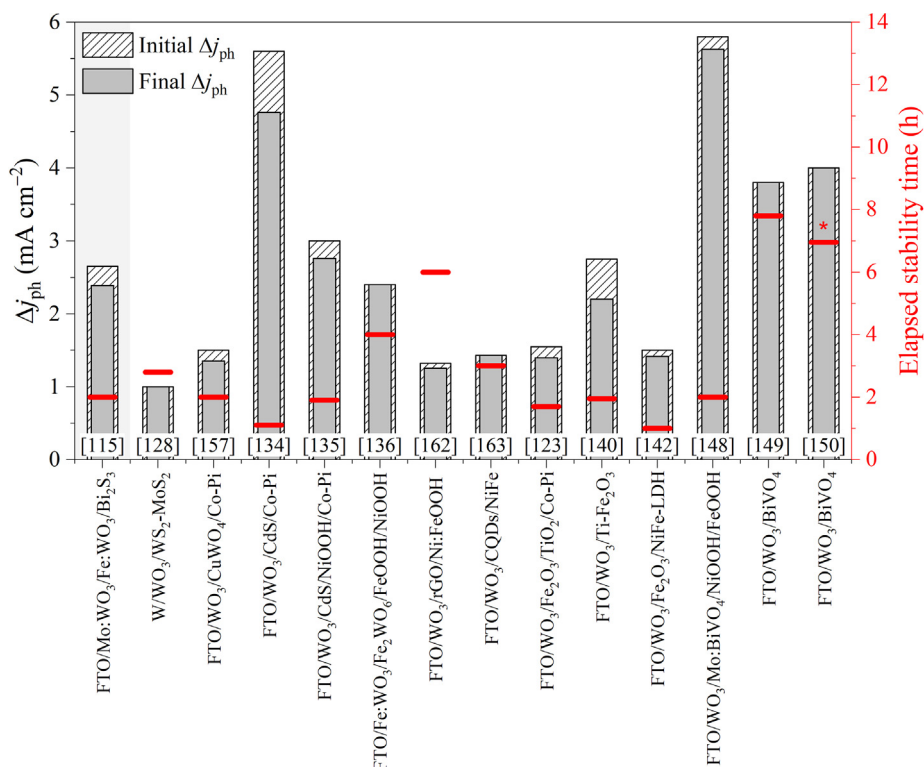
Fig. 16. Elapsed stability time and initial and final Δj_{ph} values were achieved before and after the stability test, respectively, at 1.23 V_{RHE} for the most recent homo- and heterojunction-based WO_3 photoanodes. The presented values of Δj_{ph} correspond to approximations based on the elapsed stability tests from their initial and final values. *The experiment was monitored for 24 days.

M.B. Costa, Moisés A. de Araújo, Marcos V. de Lima Tinoco et al.

Journal of Energy Chemistry 73 (2022) 88–113

[152]. Employing the nanosecond mid-IR TA experiments, it was able to confirm that charge carrier separation takes place in the $WO_3/BiVO_4$ system under visible light excitation and it persists up to the microsecond time scale. Furthermore, trapping and recombination of the photogenerated electrons in the $BiVO_4$ can be avoided by the flow of them into WO_3 where they live longer. In other words, the key role of WO_3 is to extend the photogenerated electrons' lifetime in the $WO_3/BiVO_4$ heterojunction [152].

A summary of the most recent heterostructure-based WO_3 films for PEC water splitting is shown in Table 7.

At last, aiming to seek a possible general trending of the photoresponse, i.e., Δj_{ph} at 1.23 V_{RHE}, before and after elapsed stability time for WO_3-based heterojunctions, some of the most relevant data listed in Table 7 were arranged in Fig. 16. As a reminder, the compiled PEC data in Fig. 16 is to observe a probable trend of the PEC response as a function of WO_3-heterojunctions. We have no intention of systematically comparing these data as each system has unique surface characteristics and the PEC experiments were performed under different conditions (e.g., electrolyte and power of lamps). Having that being reminded, it is possible to observe from Fig. 16 that the $FTO/WO_3/CdS/Co-Pi$ delivered one of the highest initial and final Δj_{ph} values. Despite the outstanding generated photoresponse for water splitting, such a system features as a drawback the considerable toxicity of cadmium, which goes against the idea of constructing a green photocatalyst. Another heterostructure system reviewed here with considerable Δj_{ph} response and stability is the one comprised of WO_3 and $BiVO_4$ ($WO_3/BiVO_4$). The $WO_3/BiVO_4$ heterostructure stands out to be more attractive in terms of being a green system with earth-abundant elements and having suitable optoelectronic properties for light-driven water splitting. Even with no additional junctions, the combination of WO_3 and $BiVO_4$ reached a remarkable Δj_{ph} of ca. 4.0 mA cm^{-2} at 1.23 V_{RHE} and enabled performing stability experiment for up to 8 h under continuous illumination and polarization. In this sense, the combination of other green catalysts with the $WO_3/BiVO_4$ heterostructure seems to be a promisor option to be further investigated, since the highest Δj_{ph} before and after elapsed stability time (cf. Fig. 16) was for the $FTO/WO_3/Mo:BiVO_4/NiOOH/FeOOH$ system.

4. Conclusions and perspective

The fundamental study about the improvement of the water splitting reaction to obtain renewable and sustainable energy sources is based on the development of low-cost, efficient, stable, and photoactive catalysts. For that, WO_3 semiconductor is a potential photoanode material due to its intrinsic characteristics concerning a narrow E_g in the visible range (around 2.4 eV), E_{VB} sufficiently more positive than the potential for water oxidation, resistance against photocorrosion in aqueous solutions, and a long hole diffusion length ($\sim$150 nm) [4]. However, the WO_3 semiconductor presents high recombination of the charge carries and a relatively high overpotential for water oxidation. In light of these, this review brings many recent arrangements possibilities and other strategies to improve the WO_3 efficiency. This work also aimed to review the most recent studies about the influence of the WO_3 morphology (Table 1) and crystal plane growth (Table 2), the defect engineering based on oxygen vacancies (Table 3), and the modifications, such as doping (Table 4), decorations (Table 5), and homo (Table 6) and heterojunctions (Table 7) for solar-driven water splitting application.

Most papers in the literature seek only a high Δj_{ph} and good stability, nevertheless few ones have reported on ABPE values. The latter involves both the importance of the Δj_{ph} and the E_{on} so that ABPE combined with stability would be an excellent parameter to

verify the best strategies employed. From this point of view, papers based on heterojunctions are the ones that most describe these parameters and are highlighted among the others for presenting excellent results [127,134–136,144,177,180]. However, based on the comparison of the Δj_{ph} response of a variety of WO_3-based systems for water oxidation, it is possible to infer that the combination of a desired morphology and crystal plane with a heterojunction can bring higher photoelectroactivity with good stability for water splitting reaction [148–150,186,194,197]. The improvement of water photooxidation was more pronounced when multijunctions were applied [168]. However, the choice of the second semiconductor (or more than one) that will be used in a WO_3-based heterojunction needs to be carefully considered. Some of the modifications reported in the literature caused a decrease in the Δj_{ph} reaching values that are even lower than the pure WO_3 photoanode [170,176,181,191]. In this sense, the junctions applied in the WO_3 photoanode must be adjusted to obtain an efficient energetic coupling of the band edges of all the semiconductors taking into consideration as well as the redox couple potential in the electrolyte to minimize the recombination losses or losses across the interfaces. Another important and recurring aspect in papers on photoelectrodes applied to light-driven water splitting is the lack of information and clarity about the stability data. This is one of the most relevant results in this area and is often neglected, as can be seen in this review when approaching recent works. Such data must be quantified correctly and presented clearly for possible comparison between the PECs systems. This practice is already happening in highly relevant papers and should become a priority in the presentation of data.

At last, as it is already known, engineering nanoarchitectures is a great option to increase the Δj_{ph} of photocatalysts, and it is not different for WO_3. In this regard, it is necessary to seek nanostructures and properties that can maximize the performance and reliability to obtain the most successful material, also taking into consideration the necessary junctions and modifications, which are essential for an efficient water splitting process. No less important than designing a better electrode, the optimization of the device that will be used in this reaction is extremely important, and sometimes, neglected. Only when those two points were aligned is that the solar-driven water splitting will become a real option for energy production in a large-scale process.

Declaration of Competing Interest

The authors declare that they have no known competing financial interests or personal relationships that could have appeared to influence the work reported in this paper.

Acknowledgments

References

[1] J.A. Linthorst, Found Chem 12 (2010) 55–68.
[2] Q. Ding, B. Song, P. Xu, S. Jin, Chem 1 (2016) 699–726.
[3] S. Ye, C. Ding, R. Chen, F. Fan, P. Fu, H. Yin, X. Wang, Z. Wang, P. Du, C. Li, J. Am. Chem. Soc. 140 (2018) 3250–3256.
[4] Y. Wang, W. Tian, C. Chen, W. Xu, L. Li, Adv. Funct. Mater. 29 (2019) 1809036.
[5] L.M. Peter, Chem. Rev. 90 (1990) 753–769.

[6] G. Jerkiewicz, ACS Catal. 10 (2020) 8409–8417.

[7] R. van de Krol, M. Grätzel, Photoelectrochemical Hydrogen Production, Springer, Nova York, 2012.

[8] Z. Chen, H.N. Dinh, E. Miller, Photoelectrochemical Water Splitting: Standards, Experimental Methods, and Protocols, 1st ed., Springer-Verlag, New York, New York, 2013.

[9] R.T. Ross, J. Chem. Phys. 45 (1966) 1–7.

[10] A. Murphy, P. Barnes, L. Randeniya, I. Plumb, I. Grey, M. Horne, J. Glasscock, Int. J. Hydrogen Energy 31 (2006) 1999–2017.

[11] A. Govind Rajan, J.M.P. Martirez, E.A. Carter. ACS Catal. 10. (2020). 11177–11234.

[12] J. Huang, P. Yue, L. Wang, H. She, Q. Wang, Chinese J. Catal. 40 (2019) 1408–1420.

[13] D. Sánchez Martínez, A. Martínez-de la Cruz, E. López Cuéllar, Appl. Catal. A Gen. 398 (2011) 179–186.

[14] X. Liu, F. Wang, Q. Wang, Phys. Chem. Chem. Phys. 14 (2012) 7894.

[15] X. Feng, Y. Chen, Z. Qin, M. Wang, L. Guo, ACS. Appl. Mater. Interfaces 8 (2016) 18089–18096.

[16] S. Ye, C. Ding, M. Liu, A. Wang, Q. Huang, C. Li, Adv. Mater. 31 (2019) 1902069.

[17] W.A. Smith, I.D. Sharp, N.C. Strandwitz, J. Bisquert, Energy Environ. Sci. 8 (2015) 2851–2862.

[18] G.G. Bessegato, T.T. Guaraldo, J.F. de Brito, M.F. Brugnera, M.V.B. Zanoni, Electrocatalysis 6 (2015) 415–441.

[19] G. Zheng, J. Wang, H. Liu, V. Murugadoss, G. Zu, H. Che, C. Lai, H. Li, T. Ding, Q. Gao, Z. Guo, Nanoscale 11 (2019) 18968–18994.

[20] S.A. Alves, L.L. Soares, L.A. Goulart, L.H. Mascaro, J. Solid State Electrochem. 20 (2016) 2461–2470.

[21] Á. Valdés, G.-J. Kroes, J. Chem. Phys. 130 (2009) 114701.

[22] A. Leaustic, F. Babonneau, J. Livage, J. Phys. Chem. 90 (1986) 4193–4198.

[23] M.D. Bhatt, J.S. Lee, J. Mater. Chem. A 3 (2015) 10632–10659.

[24] C. Dulgerbaki, A.U. Oksuz, in: Adv. Electrode Mater., Scrivener Publishing, 2017, pp. 61–99.

[25] G. Hodes, D. Cahen, J. Manassen, Nature 260 (1976) 312–313.

[26] M. Yang, H. He, H. Zhang, X. Zhong, F. Dong, G. Ke, Y. Chen, J. Du, Y. Zhou, Electrochim. Acta 283 (2018) 871–881.

[27] W. Kim, T. Tachikawa, D. Monllor-Satoca, H. Kim, T. Majima, W. Choi, Energy Environ. Sci. 6 (2013) 3732.

[28] J. Cen, Q. Wu, D. Yan, W. Zhang, Y. Zhao, X. Tong, M. Liu, A. Orlov, RSC Adv. 9 (2019) 899–905.

[29] X. Chen, J. Yang, Y. Cao, L. Kong, J. Huang, ChemElectroChem 8 (2021) 4427–4440.

[30] G. Hodes, P.V. Kamat, J. Phys. Chem. Lett. 6 (2015) 4090–4092.

[31] J.A. Seabold, K.-S. Choi, Chem. Mater. 23 (2011) 1105–1112.

[32] H.S. Han, W. Park, S.W. Hwang, H. Kim, Y. Sim, S. Surendran, U. Sim, I.S. Cho, J. Catal. 389 (2020) 328–336.

[33] G. Zheng, J. Wang, G. Zu, H. Che, C. Lai, H. Li, V. Murugadoss, C. Yan, J. Fan, Z. Guo, J. Mater. Chem. A 7 (2019) 26077–26088.

[34] G. Wang, Y. Ling, H. Wang, X. Yang, C. Wang, J.Z. Zhang, Y. Li, Energy Environ. Sci. 5 (2012) 6180.

[35] S.S. Kalanur, I.-H. Yoo, H. Seo, Electrochim. Acta 254 (2017) 348–357.

[36] M. Dahl, Y. Liu, Y. Yin, Chem. Rev. 114 (2014) 9853–9889.

[37] L. Pan, S. Wang, J. Xie, L. Wang, X. Zhang, J.-J. Zou, Nano Energy 28 (2016) 296–303.

[38] N. Wang, M. Liu, H. Tan, J. Liang, Q. Zhang, C. Wei, Y. Zhao, E.H. Sargent, X. Zhang, Small 13 (2017) 1603527.

[39] M.K. Sanyal, A. Datta, S. Hazra, Pure Appl. Chem. 74 (2002) 1553–1570.

[40] T. Li, J. He, B. Peña, C.P. Berlinguette, ACS Appl. Mater. Interfaces 8 (2016) 25010–25013.

[41] Y. Li, J.Z. Zhang, Laser Photon. Rev. 4 (2009) 517–528.

[42] G. Wang, Y. Ling, H. Wang, L. Xihong, Y. Li, J. Photochem. Photobiol. C Photochem. Rev. 19 (2014) 35–51.

[43] F.E. Osterloh, Chem. Soc. Rev. 42 (2013) 2294–2320.

[44] T. Zhang, M. Paulose, R. Neupane, L.A. Schaffer, D.B. Rana, J. Su, L. Guo, O.K. Varghese, Sol. Energy Mater. Sol. Cells 209 (2020) 110472.

[45] G. Roselló-Márquez, R.M. Fernández-Domene, R. Sánchez-Tovar, J. García-Antón, Sep. Purif. Technol. 238 (2020) 116417.

[46] Y. Gu, W. Zheng, Y. Bu, J. Electroanal. Chem. 833 (2019) 54–62.

[47] L.-D. Zhao, Q. Zhang, J.-B. Fan, L.-Q. Yin, P.-W. Qi, H.-C. Yao, Z.-J. Li, J. Solid State Electrochem. 23 (2019) 1621–1630.

[48] Y.-Q. Rong, X.-F. Yang, W.-D. Zhang, Y.-X. Yu, Mater. Lett. 246 (2019) 161–164.

[49] J. Feng, X. Zhao, B. Zhang, G. Yang, Q. Qian, S.S.K. Ma, Z. Chen, Z. Li, Y. Huang, Sci. China Mater. 63 (2020) 2261–2271.

[50] Y. Wang, F. Zhang, G. Zhao, Y. Zhao, Y. Ren, H. Zhang, L. Zhang, J. Du, Y. Han, D. J. Kang, Ceram. Int. 45 (2019) 7302–7308.

[51] M. Jadwiszczak, K. Jakubow-Piotrowska, P. Kedzierzawski, K. Bienkowski, J. Augustynski, Adv. Energy Mater. 10 (2020) 1903213.

[52] F. Andrei, A. Andrei, R. Birjega, E.N. Sirjita, A.I. Radu, M. Dinescu, V. Ion, V.-A. Maraloiu, V.Ș. Teodorescu, N.D. Scarisoreanu, Nanomaterials 11 (2021) 110.

[53] M. Stefik, M. Cornuz, N. Mathews, T. Hisatomi, S. Mhaisalkar, M. Grätzel, Nano Lett. 12 (2012) 5431–5435.

[54] D. Chandra, K. Saito, T. Yui, M. Yagi, Angew. Chemie Int. Ed. 52 (2013) 12606–12609.

[55] M. Rodríguez-Pérez, I. Rodríguez-Gutiérrez, A. Vega-Poot, R. García-Rodríguez, G. Rodríguez-Gattorno, G. Oskam, Electrochim. Acta 258 (2017) 900–908.

[56] D.P. Norton, in: Pulsed Laser Depos. Thin Film, John Wiley & Sons Inc, Hoboken, NJ, USA, 2006, pp. 1–31.

[57] D. Chandra, D. Li, T. Sato, Y. Tanahashi, T. Togashi, M. Ishizaki, M. Kurihara, E. A. Mohamed, Y. Tsubonouchi, Z.N. Zahran, K. Saito, T. Yui, M. Yagi, A.C.S. Sustain, Chem. Eng. 7 (2019) 17896–17906.

[58] N. Kangkun, N. Kiama, N. Saito, C. Ponchio, Optik (Stuttg). 198 (2019) 163235.

[59] Y. Feng, L. Guan, J. Li, X. Li, S. Zhang, Y. Jiao, S. Zhang, Y. Lin, Y. Ren, X. Zhou, Z. Liu, J. Mater. Sci. Mater. Electron. 31 (2020) 14137–14144.

[60] J. Kim, H. Lee, J.H. Choi, C. Park, B. Lee, J.Y. Jung, J.H. Park, J. Lee, S.J. Cho, Nanotechnology 32 (2021) 395402.

[61] Y. Shabdan, A. Markhabayeva, N. Bakranov, N. Nuraje, Nanomaterials 10 (2020) 1871.

[62] N. Wang, D. Wang, M. Li, J. Shi, C. Li, Nanoscale 6 (2014) 2061–2066.

[63] S.S. Kalanur, Y.J. Hwang, S.Y. Chae, O.S. Joo, J. Mater. Chem. A 1 (2013) 3479–3488.

[64] J.Y. Zheng, G. Song, C.W. Kim, Y.S. Kang, Nanoscale 5 (2013) 5279.

[65] R. Kishore, X. Cao, X. Zhang, A. Bieberle-Hütter, Catal. Today 321–322 (2019) 94–99.

[66] J. Zhou, Y. Ding, S.Z. Deng, L. Gong, N.S. Xu, Z.L. Wang, Adv. Mater. 17 (2005) 2107–2110.

[67] H.V. Le, P.T. Pham, L.T. Le, A.D. Nguyen, N.Q. Tran, P.D. Tran, Int. J. Hydrogen Energy 46 (2021) 22852–22863.

[68] Y. Zhao, S. Balasubramanyam, R. Sinha, R. Lavrijsen, M.A. Verheijen, A.A. Bol, A. Bieberle-Hütter, ACS Appl. Energy Mater. 1 (2018) 5887–5895.

[69] L. Ma, S. Chen, Z. Pei, H. Li, Z. Wang, Z. Liu, Z. Tang, J.A. Zapien, C. Zhi, ACS Nano 12 (2018) 8597–8605.

[70] S. Rahimnejad, J. Hui He, F. Pan, X. Lee, W. Chen, K. Wu, G. Qin Xu, Mater. Res. Express 1 (2014) 045044.

[71] Q. Liu, F. Wang, H. Lin, Y. Xie, N. Tong, J. Lin, X. Zhang, Z. Zhang, X. Wang, Catal. Sci. Technol. 8 (2018) 4399–4406.

[72] M. Ma, K. Zhang, P. Li, M.S. Jung, M.J. Jeong, J.H. Park, Angew. Chemie Int. Ed. 55 (2016) (1823) 11819–11823.

[73] G. Wang, H. Wang, Y. Ling, Y. Tang, X. Yang, R.C. Fitzmorris, C. Wang, J.Z. Zhang, Y. Li, Nano Lett. 11 (2011) 3026–3033.

[74] G. Wang, Y. Yang, Y. Ling, H. Wang, X. Lu, Y.-C. Pu, J.Z. Zhang, Y. Tong, Y. Li, J. Mater. Chem. A 4 (2016) 2849–2855.

[75] I.S. Cho, M. Logar, C.H. Lee, L. Cai, F.B. Prinz, X. Zheng, Nano Lett. 14 (2014) 24–31.

[76] Y. Liu, L. Kong, X. Guo, J. Xu, S. Shi, L. Li, J. Phys. Chem. Solids 149 (2021) 109823.

[77] C. Shao, A.S. Malik, J. Han, D. Li, M. Dupuis, X. Zong, C. Li, Nano Energy 77 (2020) 105190.

[78] S.S. Kalanur, I.-H. Yoo, I.-S. Cho, H. Seo, Electrochim. Acta 296 (2019) 517–527.

[79] T. Soltani, A. Tayyebi, H. Hong, M.H. Mirfasih, B.-K. Lee, Sol. Energy Mater. Sol. Cells 191 (2019) 39–49.

[80] S. Hoang, S. Guo, N.T. Hahn, A.J. Bard, C.B. Mullins, Nano Lett. 12 (2012) 26–32.

[81] S.-M. Tao, L.-Y. Lin, Int. J. Hydrogen Energy 45 (2020) 6487–6499.

[82] S. Shen, J. Zhou, C.-L. Dong, Y. Hu, E.N. Tseng, P. Guo, L. Guo, S.S. Mao, Sci. Rep. 4 (2015) 6627.

[83] S.S. Kalanur, I.-H. Yoo, K. Eom, H. Seo, J. Catal. 357 (2018) 127–137.

[84] F. Wang, C. Di Valentin, G. Pacchioni, J. Phys. Chem. C 116 (2012) 8901–8909.

[85] M. Kumar Mohanta, T. Kanta Sahu, S. Alam, M. Qureshi, Chem. – An Asian J. 15 (2020) 3886–3896.

[86] S.S. Kalanur, Y.-G. Noh, H. Seo, Appl. Surf. Sci. 509 (2020) 145253.

[87] X. Yin, W. Qiu, W. Li, K. Wang, X. Yang, L. Du, Y. Liu, J. Li, Int. J. Hydrogen Energy 45 (2020) 19257–19266.

[88] S.S. Kalanur, H. Seo, J. Alloys Compd. 785 (2019) 1097–1105.

[89] S.S. Kalanur, Catalysts 9 (2019) 456.

[90] S.S. Kalanur, I.-H. Yoo, I.S. Cho, H. Seo, Ceram. Int. 45 (2019) 8157–8165.

[91] Y. Ma, Y.H. Hu, Appl. Phys. Lett. 118 (2021) 223903.

[92] C. Ros, T. Andreu, J.R. Morante, J. Mater. Chem. A 8 (2020) 10625–10669.

[93] W. Xu, W. Tian, L. Li, Sol. RRL (2020) 2000412.

[94] H. Gerischer, J. Vac. Sci. Technol. 15 (1978) 1422–1428.

[95] H. Gerischer, in: Sol. Energy Convers. Solid-State Phys. Asp., Springer, 1979, pp. 117–172.

[96] C.R. Lhermitte, J. Garret Verwer, B.M. Bartlett, J. Mater. Chem. A 4 (2016) 2960–2968.

[97] D.R. Lide (Ed.), CRC Handbook of Chemistry and Physics, 89th ed., CRC Press, Boca Raton, 2008.

[98] J. Jun, S. Ju, S. Moon, S. Son, D. Huh, Y. Liu, K. Kim, H. Lee, Nanotechnology 31 (2020) 204003.

[99] R. Solarska, A. Królikowska, J. Augustyński, Angew. Chemie Int. Ed. 49 (2010) 7980–7983.

[100] A.A. Wilson, S. Corby, L. Francàs, J.R. Durrant, A. Kafizas, Phys. Chem. Chem. Phys. 23 (2021) 1285–1291.

[101] M.K. Mohanta, T.K. Sahu, D. Gogoi, N.R. Peela, M. Qureshi, ACS Appl. Energy Mater. 2 (2019) 7457–7466.

[102] Y. Li, W. Zhang, B. Qiu, Chem. Lett. 49 (2020) 741–744.

[103] Y. Liu, Y.-S. Chang, Y.-J. Hsu, B.-J. Hwang, C.-H. Hsueh, Electrochim. Acta 321 (2019) 134674.

[104] Y. Li, Z. Liu, Z. Guo, M. Ruan, X. Li, Y. Liu, A.C.S. Sustain, Chem. Eng. 7 (2019) 12582–12590.

[105] B.-E. Wu, C.-Y. Chiang, J. Taiwan Inst. Chem. Eng. 80 (2017) 1014–1021.

[106] P. Schnell, M. Kölbach, M. Schleuning, K. Obata, R. Irani, I.Y. Ahmet, M. Harb, D.E. Starr, R. van de Krol, F.F. Abdi, Adv. Energy Mater. 11 (2021) 2003183.

[107] Y.P. Xie, G. Liu, G.Q. (Max) Lu, H.-M. Cheng, Nanoscale 4 (2012) 1267.
[108] H. Zhang, C. Guo, J. Ren, J. Ning, Y. Zhong, Z. Zhang, Y. Hu, Chem. Commun. 55 (2019) 14050–14053.
[109] G.-L. Hu, R. Hu, Z.-H. Liu, K. Wang, X.-Y. Yan, H.-Y. Wang, Catal. Sci. Technol. 10 (2020) 5677–5687.
[110] P. Chatterjee, A.K. Chakraborty, Opt. Mater. (Amst). 111 (2021) 110610.
[111] B. Jin, Y. Cho, Y. Zhang, D.H. Chun, P. Li, K. Zhang, K.-S. Lee, J.H. Park, Nano Energy 66 (2019) 104110.
[112] W. Kong, X. Zhang, S. Liu, Y. Zhou, B. Chang, S. Zhang, H. Fan, B. Yang, Adv. Mater. Interfaces 6 (2019) 1801653.
[113] M. Ertl, Z. Ma, T. Thersleff, P. Lyu, S. Huettner, P. Nachtigall, J. Breu, A. Slabon, Inorg. Chem. 58 (2019) 9655–9662.
[114] J. Liu, Z. Shang, J. Chen, L. Wen, J. Liu, Catal. Letters (2021), https://doi.org/10.1007/s10562-021-03856-6.
[115] Y. Li, Z. Liu, J. Li, M. Ruan, Z. Guo, J. Mater. Chem. A 8 (2020) 6256–6267.
[116] Z. Ma, H. Hou, K. Song, Z. Fang, L. Wang, F. Gao, W. Yang, B. Tang, Y. Kuang, Chem. Eng. J. 379 (2020) 122266.
[117] Y. Li, Z. Liu, M. Ruan, Z. Guo, X. Li, ChemSusChem 12 (2019) 5282–5290.
[118] M. Yang, J. Li, G. Ke, B. Liu, F. Dong, L. Yang, H. He, Y. Zhou, J. Energy Chem. 56 (2021) 37–45.
[119] Y. Tian, B. Chang, J. Lu, J. Fu, F. Xi, X. Dong, ACS Appl. Mater. Interfaces 5 (2013) 7079–7085.
[120] K. Afroz, M. Moniruddin, N. Bakranov, S. Kudaibergenov, N. Nuraje, J. Mater. Chem. A 6 (2018) 21696–21718.
[121] S.J.A. Moniz, S.A. Shevlin, D.J. Martin, Z.-X. Guo, J. Tang, Energy Environ. Sci. 8 (2015) 731–759.
[122] X. Su, C. Liu, Y. Liu, Y. Yang, X. Liu, S. Chen, Trans. Nonferrous Met. Soc. China 31 (2021) 533–544.
[123] E. Kim, S. Kim, Y.M. Choi, J.H. Park, H. Shin, A.C.S. Sustain, Chem. Eng. 8 (2020) 11358–11367.
[124] C.-H. Wang, D.-D. Qin, D.-L. Shan, J. Gu, Y. Yan, J. Chen, Q.-H. Wang, C.-H. He, Y. Li, J.-J. Quan, X.-Q. Lu, Phys. Chem. Chem. Phys. 19 (2017) 4507–4515.
[125] J. Zhang, H. Ma, Z. Liu, Appl. Catal. B Environ. 201 (2017) 84–91.
[126] R. Wang, T. Xie, T. Zhang, T. Pu, Y. Bu, J.-P. Ao, J. Mater. Chem. A 6 (2018) 12956–12961.
[127] M. Tayebi, Z. Masoumi, B.-K. Lee, Ultrason. Sonochem. 70 (2021) 105339.
[128] M. Mojaddami, A. Simchi, Renew. Energy 162 (2020) 504–512.
[129] C.T. Moi, G. Gogoi, T.K. Sahu, D. Gogoi, N.R. Peela, M. Qureshi, Sustain, Energy Fuels 3 (2019) 3481–3488.
[130] Y. Qu, M. Shao, Y. Shao, M. Yang, J. Xu, C.T. Kwok, X. Shi, Z. Lu, H. Pan, J. Mater. Chem. A 5 (2017) 15080–15086.
[131] M.G. Hosseini, P.Y. Sefidi, Z. Aydin, S. Kinayyigit, Electrochim. Acta 333 (2020) 135475.
[132] M.G. Hosseini, P.Y. Sefidi, S. Kinayyigit, Mater. Sci. Semicond. Process. 121 (2021) 105440.
[133] S. Yoo, J. Kum, G. Ali, S. Heo, S. Cho, Nanoscale Res. Lett. 7 (2012) 142.
[134] J. Sun, L. Sun, X. Yang, S. Bai, R. Luo, D. Li, A. Chen, Electrochim. Acta 331 (2020) 135282.
[135] Y. Li, Z. Liu, J. Zhang, Z. Guo, Y. Xin, L. Zhao, J. Alloys Compd. 790 (2019) 493–501.
[136] H. Lin, X. Long, Y. An, S. Yang, J. Chem. Phys. 152 (2020) 214704.
[137] W. Ma, X. Wu, K. Huang, M. Wang, R. Fu, H. Chen, S. Feng, Sustain. Energy Fuels 3 (2019) 2135–2141.
[138] H. Dotan, O. Kfir, E. Sharlin, O. Blank, M. Gross, I. Dumchin, G. Ankonina, A. Rothschild, Nat. Mater. 12 (2013) 158–164.
[139] J. Li, S.K. Cushing, P. Zheng, F. Meng, D. Chu, N. Wu, Nat. Commun. 4 (2013) 2651.
[140] Q. Wu, Q. Bu, S. Li, Y. Lin, X. Zou, D. Wang, T. Xie, J. Alloys Compd. 803 (2019) 1105–1111.
[141] T.T. Guaraldo, J.F. Brito, D. Wood, M.V.B. Zanoni, Electrochim. Acta 185 (2015) 117–124.
[142] X. Fan, T. Wang, H. Xue, B. Gao, S. Zhang, H. Gong, H. Guo, L. Song, W. Xia, J. He, ChemElectroChem 6 (2019) 543–551.
[143] S. Ye, W. Shi, Y. Liu, D. Li, H. Yin, H. Chi, Y. Luo, N. Ta, F. Fan, X. Wang, C. Li, J. Am. Chem. Soc. 143 (2021) 12499–12508.
[144] S.-H. Yoon, T. Sadike, J.-R. Ding, K.-S. Kim, J. Ind. Eng. Chem. 85 (2020) 240–248.
[145] T.W. Kim, K.-S. Choi, Science (80-.) 343 (2014) 990–994.
[146] B. Chen, Z. Zhang, M. Baek, S. Kim, W. Kim, K. Yong, Appl. Catal. B Environ. 237 (2018) 763–771.
[147] Z. Ma, K. Song, L. Wang, F. Gao, B. Tang, H. Hou, W. Yang, ACS Appl. Mater. Interfaces 11 (2019) 889–897.
[148] K. Kim, S.K. Nam, J.H. Park, J.H. Moon, J. Mater. Chem. A 7 (2019) 4480–4485.
[149] B.R. Lee, M.G. Lee, H. Park, T.H. Lee, S.A. Lee, S.S.M. Bhat, C. Kim, S. Lee, H.W. Jang, ACS Appl. Mater. Interfaces 11 (2019) 20004–20012.
[150] J.-H. Kim, D.H. Kim, J.W. Yoon, Z. Dai, J.-H. Lee, ACS Appl. Energy Mater. 2 (2019) 4535–4543.
[151] D. Coelho, J.P.R.S. Gaudêncio, S.A. Carminati, F.W.P. Ribeiro, A.F. Nogueira, L.H. Mascaro, Chem. Eng. J. 399 (2020) 125836.
[152] I. Grigioni, M. Abdellah, A. Corti, M.V. Dozzi, L. Hammarström, E. Selli, J. Am. Chem. Soc. 140 (2018) 14042–14045.
[153] W. Tian, C. Chen, L. Meng, W. Xu, F. Cao, L. Li, Adv. Energy Mater. 10 (2020) 1903951.
[154] Y. Wang, C. Chen, W. Tian, W. Xu, L. Li, Nanotechnology 30 (2019) 495402.
[155] X. Shi, F. Dong, C. Dai, X. Ye, P. Yang, L. Zheng, H. Zheng, Electrochim. Acta 361 (2020) 137017.
[156] T. Wang, X. Fan, B. Gao, C. Jiang, Y. Li, P. Li, S. Zhang, X. Huang, J. He, ChemElectroChem 8 (2021) 125–134.
[157] Z. Hao, Z. Liu, Y. Li, M. Ruan, Z. Guo, Int. J. Hydrogen Energy 45 (2020) 16550–16559.
[158] J. Liu, Q. Yang, J. Liu, H. Luo, J. Mater. Sci. 56 (2021) 8079–8090.
[159] Z. Chen, A.J. Corkett, C. de Bruin-Dickason, J. Chen, A. Rokicińska, P. Kuśtrowski, R. Dronskowski, A. Slabon, Inorg. Chem. 59 (2020) 13589–13597.
[160] Z. Hao, Z. Guo, M. Ruan, J. Ya, Y. Yang, X. Wu, Z. Liu, ChemCatChem 13 (2021) 271–280.
[161] Y. Ma, Y.H. Hu, J. Phys. Chem. C 124 (2020) 19447–19456.
[162] X. Zhang, X. Bian, H. Xu, W. Wu, Appl. Surf. Sci. 542 (2021) 148579.
[163] X. Cao, C. Xu, J. Ma, Y. Dong, C. Dong, M. Yue, Y. Ding, ChemSusChem 12 (2019) 4685–4692.
[164] Y.-F. Zhang, Y.-K. Zhu, C.-X. Lv, S.-J. Lai, W.-J. Xu, J. Sun, Y.-Y. Sun, D.-J. Yang, Rare Met. 39 (2020) 841–849.
[165] J. Zhang, G. Zhu, W. Liu, Y. Xi, D.A. Golosov, S.M. Zavadski, S.N. Melnikov, J. Alloys Compd. 834 (2020) 154992.
[166] X. Zhang, X. Wang, D. Wang, J. Ye, ACS Appl. Mater. Interfaces 11 (2019) 5623–5631.
[167] Y. Liu, B.R. Wygant, K. Kawashima, O. Mabayoje, T.E. Hong, S.-G. Lee, J. Lin, J.-H. Kim, K. Yubuta, W. Li, J. Li, C.B. Mullins, Appl. Catal. B Environ. 245 (2019) 227–239.
[168] S. Khoomortezaei, H. Abdizadeh, M.R. Golobostanfard, ACS Appl. Energy Mater. 2 (2019) 6428–6439.
[169] V.O. Smilyk, S.S. Fomanyuk, G.Y. Kolbasov, I.A. Rusetskyi, V.S. Vorobets, Res. Chem. Intermed. 45 (2019) 4149–4161.
[170] L. Zhou, Y. Wu, L. Wang, Y. Yang, Y. Na, Inorg. Chem. Commun. 107 (2019) 107480.
[171] I. Grigioni, L. Ganzer, F.V.A. Camargo, B. Bozzini, G. Cerullo, E. Selli, ACS Energy Lett. 4 (2019) 2213–2219.
[172] Q. Pan, H. Zhang, Y. Yang, C. Cheng, Small 15 (2019) 1900924.
[173] V.S. Kumbhar, H. Lee, J. Lee, K. Lee, J. Colloid Interface Sci. 557 (2019) 478–487.
[174] L. Zhang, M. Yang, Z. Luo, J. Zhang, Y. Hou, Int. J. Hydrogen Energy 44 (2019) 25652–25661.
[175] S. Ju, H.-J. Seok, J. Jun, D. Huh, S. Son, K. Kim, W. Kim, S. Baek, H.-K. Kim, H. Lee, Appl. Catal. B Environ. 263 (2020) 118362.
[176] S. Phiankoh, P. Prajongtat, M. Chareonpanich, R. Munprom, Energy Technol. 8 (2020) 2000147.
[177] H. Sun, H. Wua, Y. Li, J.-G. Wang, A.C.S. Sustain, Chem. Eng. 8 (2020) 12637–12645.
[178] S.D. Ghadge, M.K. Datta, O.I. Velikokhatnyi, P.N. Kumta, Int. J. Hydrogen Energy 47 (2022) 993–1005.
[179] J.H. Kim, J.W. Yoon, T.H. Kim, Y.M. Jo, J.S. Kim, S.Y. Jeong, J.H. Lee, Chem. Eng. J. 425 (2021) 131496.
[180] A. Singh, S. Karmakar, S. Basu, Int. J. Hydrogen Energy 46 (2021) 39868–39881.
[181] J. Ji, P. Sang, J.H. Kim, Ceram. Int. 47 (2021) 26260–26270.
[182] M.S. Sayed, D. Mohapatra, M.L. Baynosa, J.J. Shim, J. Colloid Interface Sci. 598 (2021) 348–357.
[183] E. Park, S.S. Patil, H. Lee, V.S. Kumbhar, K. Lee, Nanoscale 13 (2021) 16932–16941.
[184] J. Feng, H. Huang, W. Guo, X. Xu, Y. Yao, Z. Yu, Z. Li, Z. Zou, Chem. Eng. J. 417 (2021) 128095.
[185] J. Li, C. Guo, L. Li, Y. Gu, K. BoK-Hee, J. Huang, Catal. Letters 152 (2022) 1611–1620.
[186] M. Sun, R.T. Gao, J. He, X. Liu, T. Nakajima, X. Zhang, L. Wang, Angew. Chemie – Int. Ed. 60 (2021) 17601–17607.
[187] V. Madhavi, P. Kondaiah, H. Shaik, K.N. Kumar, T.S.S. Kumar Naik, G.M. Rao, P. C. Ramamurthy, Mater. Chem. Phys. 274 (2021) 125095.
[188] D.B. Seo, S. Yoo, V. Dongquoc, T.N. Trung, E.T. Kim, J. Alloys Compd. 888 (2021) 161587.
[189] Q. Zhao, Z. Liu, J. Li, W. Yan, J. Ya, X. Wu, Int. J. Hydrogen Energy 46 (2021) 36113–36123.
[190] J. Wang, T. Zhou, Y. Zhang, S. Chen, J. Bai, J. Li, H. Zhu, B. Zhou, J. Colloid Interface Sci. 600 (2021) 828–837.
[191] H. Wu, Q. Liu, L. Zhang, Y. Tang, G. Wang, G. Mao, ACS Appl. Energy Mater. 4 (2021) 12508–12514.
[192] M.-J. Choi, T.L. Kim, K.S. Choi, W. Sohn, T.H. Lee, S.A. Lee, H. Park, S.Y. Jeong, J. W. Yang, S. Lee, H.W. Jang, ACS Appl. Mater. Interfaces 14 (2022) 7788–7795.
[193] J. Divya, S. Prakash, P. Saxena, S. Kumar, A.M. Dass, R.S. Kannan, J. Appl. Electrochem. 52 (2022) 535–558.
[194] U. Prasad, J.L. Young, J.C. Johnson, D.L. McGott, H. Gu, E. Garfunkel, A.M. Kannan, J. Mater. Chem. A 9 (2021) 16137–16149.
[195] C.X.M. Ta, Y. Furusho, F. Amano, Appl. Surf. Sci. 548 (2021) 149251.
[196] W. Lin, Y. Yu, Y. Fang, J. Liu, X. Li, J. Wang, Y. Zhang, C. Wang, L. Wang, X. Yu, Langmuir 37 (2021) 6490–6497.
[197] M.A. Khalifa, L. Shen, J. Zheng, C. Xu, RSC Adv. 11 (2021) 13513–13520.
[198] M. Wang, Q. Zeng, S. Chang, S. Li, C. Hu, Z. Chen, Phys. Chem. Chem. Phys. 23 (2021) 8241–8245.
[199] J. Liu, W. Chen, Q. Sun, Y. Zhang, X. Li, J. Wang, C. Wang, Y. Yu, L. Wang, X. Yu, ACS Appl. Energy Mater. 4 (2021) 2864–2872.